Supplementary Information for

Unveiling Electrode-Electrolyte Design-Based NO Reduction for NH_3 Synthesis

DongYeon Kim[†], Dongyup Shin[‡], Juheon Heo[§], Hyungseob Lim[†], Jung-Ae Lim[†], Hyung Mo Jeong[⊥], Beom-Sik Kim[†], Iljeong Heo[†], Inhwan Oh[†], Boreum Lee[§], Monika Sharma[§], Hankwon Lim[§], Hyungjun Kim[‡*], Youngkook Kwon[§*]*

[†]Center for Environment & Sustainable Resources, Korea Research Institute of Chemical Technology, Daejeon 34114, Republic of Korea

[‡]Department of Chemistry, Korea Advanced Institute of Science and Technology, Daejeon 34141, Republic of Korea

[§]School of Energy and Chemical Engineering; and Emergent Hydrogen Technology R&D Center, Ulsan National Institute of Science and Technology, Ulsan 44919, Republic of Korea

[⊥]School of Mechanical Engineering, Sungkyunkwan University, Suwon 16419, Republic of Korea

*Correspondence: hklim@unist.ac.kr, linus16@kaist.ac.kr, ykwon@unist.ac.kr

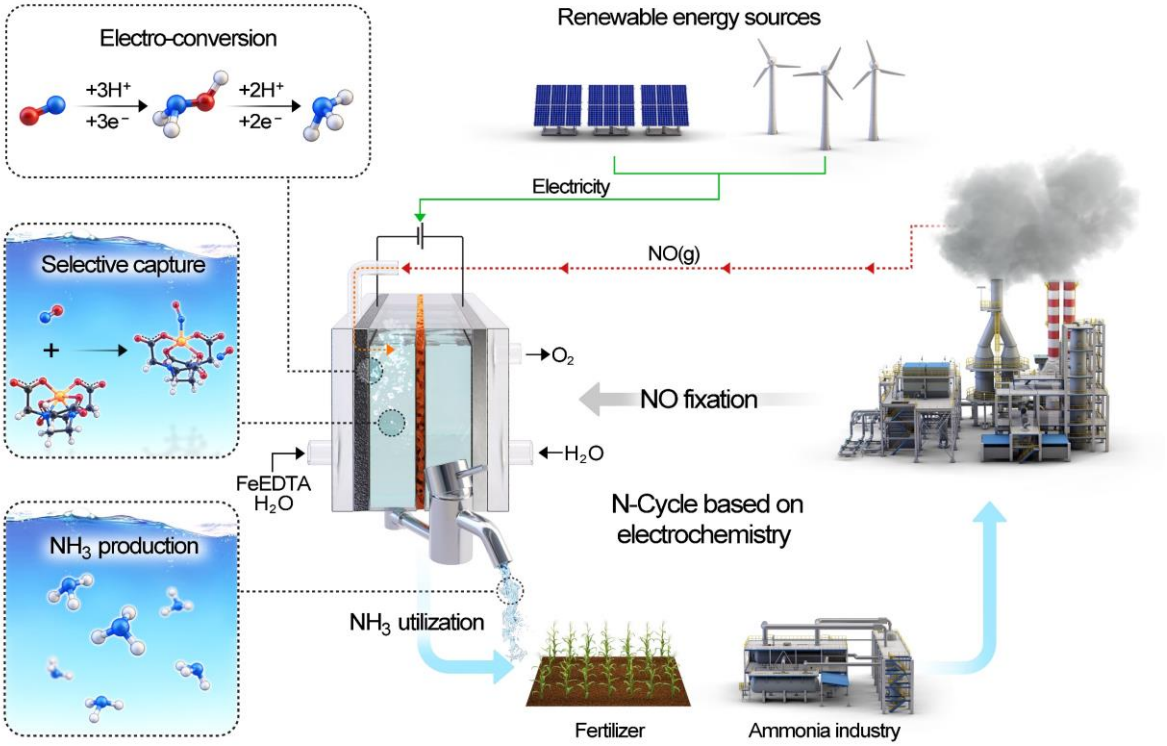

Scheme S1. Schematic illustration of the proof-of-concept-electrochemical ammonia synthesis via reduction of nitric oxide in EFeMC designed electrolyte in combination with nanostructured Ag cathode and its cycle.

Experimental Procedure

Materials

Iron (II) sulfate heptahydrate ($FeSO_4 \cdot 7H_2O$, >99%, Sigma-Aldrich), ethylenediamine-tetraacetic acid dipotassium salt dehydrate ($K_2EDTA \cdot 2H_2O$, >99.0%, Sigma-Aldrich), potassium phosphate monobasic (KH_2PO_4 99.95%, trace metals basis, Sigma-Aldrich), potassium phosphate dibasic (K_2HPO_4, 99.99%, trace metals basis, Sigma-Aldrich), potassium chloride (KCl, 99.999%, Sigma-Aldrich), potassium bicarbonate ($KHCO_3$, 99.99%), potassium hydroxide (KOH, >99.99%, Sigma-Aldrich), Pt foil (0.1 mm thickness, 99.99%, Sigma-Aldrich), Ag foil (0.1 mm thickness, 99.998%, Alfa Aesar), glassy carbon (GC, 3 mm thickness, HTW, Germany), an anion exchange membrane (Selemion AMV, Asahi Glass Co.), a 1 mm OD Ag/AgCl reference electrode (Innovative Instruments, Inc., Leak free series). 6N-Ar and NO gases with concentration of 1% and 99.9% were purchased from Rigas (Korea).

Preparation of EFeMC designed electrolyte

First, 0.5 M phosphate buffer solution (PBS) having pH 7.0 was prepared by adding 0.5 M K_2HPO_4 and 0.5 M KH_2PO_4 in a ratio of 6.15:3.85 (v/v). Then, equimolar amounts (0.05 M) of $FeSO_4 \cdot 7H_2O$ and $K_2EDTA \cdot 2H_2O$ were added to 0.5 M PBS under anaerobic conditions for the formation of EDTA-Fe^{2+} metal complex (EFeMC) in the electrolyte. For electrolyte designing, it is necessary to maintain an oxygen-free atmosphere as it prevents oxidation of Fe^{2+} into Fe^{3+} in EFeMC which can reduce its NO-binding ability. Finally, EFeMC designed electrolyte was saturated with NO by purging purified NO gas for 1 h at a flow rate of 10 sccm. NO was supplied after purification by bubbling it in 1 M KOH solution to remove impurities such as nitrogen dioxide and nitrous oxide. NO saturated and Ar gas purged EFeMC designed PBS electrolyte were termed as PBS-MC_x-NO_s and PBS-MC_x-Ar, respectively, where x denotes the concentration (mM) of EFeMC in PBS. The PBS without EFeMC additive (blank

electrolyte) purged with Ar gas and NO gas with constant flow (5 sccm) were termed as PBS-Ar and PBS-NO, respectively.

Electrochemical cell configuration

All electrochemical reactions were conducted in an H-cell configuration (**Figure S1**) consisting of a Pt foil as counter electrode, an anion exchange membrane (AEM), a 1 mm OD Ag/AgCl reference electrode, and different types of working electrodes. Pt foil, Ag foil and GC were chosen as the working electrodes and cut into 2 cm × 2 cm pieces and mechanically polished before use. The Pt foil was flame annealed additionally after mechanical polishing. The anodic and cathodic chambers with working volume of 1.5 mL were separated by an AEM, and a carrier gas (99.9999% Ar or 99.9% NO) was introduced from the bottom of the cell via a quartz micro-diffuser, which was then carried into the online gas chromatography system along with the gaseous products generated from the electrochemical reactions. The active geometric area of the working and counter electrodes was 1 cm^2.

Electrochemical performance of EFeMC designed electrolyte

All electrochemical analyses were performed using an electrochemical workstation (Biologic SP-300 Potentiostat). Potentiostatic electrochemical impedance spectroscopy (PEIS) was performed to determine the total uncompensated resistance (Ru) by applying frequencies from 5 Hz to 1 MHz at an open circuit potential. The potentiostat compensated for 85% of Ru in situ, and the remaining 15% was post-corrected to achieve accurate potentials. The applied potentials were rescaled to the reversible hydrogen electrode (RHE) after the iR compensation as per relation:

$$E_{RHE} = E_{Ag/AgCl} + 0.197\ V + 0.0591 \times pH$$

Linear sweep voltammograms (LSVs) for NORR in PBS-MC_x-NO_s were obtained at a scan rate of 20 mV s^{-1}, unless otherwise specified. Before measurements, Ar gas was bubbled into the cathodic chamber for at least 15 min and was stopped during the electrochemical tests. From the LSV results, the potential windows at which CA experiments would be performed were determined. A static reduction potential was applied for 1 h by purging with Ar gas at a flow rate of 5 sccm in PBS-MC_x-Ar. Hydrogen was the only product of the electrolysis of EFeMC, with nearly 100% H_2 Faradaic efficiencies for all the working electrodes tested at -0.2, -0.4, and -0.6 V_{RHE} on Pt foil, Ag foil, and GC cathodes, respectively.

Fabrication of nanostructured silver electrode

A nanostructured silver (Agn) electrode was synthesized by a modified chlorination-dechlorination method (Figure 3a**)**.[1] In short, Ag foil of size 3 × 5 cm^2 was mechanically polished using 1.0 µm and 0.3 µm alumina suspensions sequentially and sonicated in an isopropanol (IPA) solution for 30 min. The clean Ag foil was then chlorinated electrochemically under a constant potential of 0.3 V vs. Ag/AgCl in an Ar-saturated 0.1 M KCl solution for 12 h. The obtained dark, chlorinated film was washed with DI water several times and dried at room temperature under ambient atmosphere. To reduce the prepared AgCl film, a constant potential of -2.0 V vs. Ag/AgCl was applied to the sample in a CO_2-saturated 0.1 M $KHCO_3$ solution for 5 h. The electrochemical experiments shown in Fig. 3 were performed using the same potentiostatic equipment, gas flow conditions, and product analysis procedures as those used for the foil-type working electrodes. The double layer capacitances of the fabricated electrodes were determined by the conventional cyclic voltammetry technique. In short, cyclic voltammograms of the Ag foil and Agn electrodes were obtained in the non-

Faradaic region at different scan rates, and the capacitance was calculated by plotting the scan rates against the obtained current densities.

Characterization of electrodes

The morphologies of the prepared nanostructured Agn electrodes were examined by scanning electron microscopy (SEM) using a JEOL-JSM 6700F instrument (Nanoscope; Digital Instruments) equipped with a J scanner. X-ray diffraction (XRD) analysis was performed using a Rigaku D/Max-2200V X-ray diffractometer in the 2θ range of 5º–80º with Cu Kα radiation (λ=1.5406 nm) at 40 kV and 100 mA. X-ray photoelectron spectroscopy (XPS) was performed for the prepared samples on a Kratos AXIS Nova X-ray photoelectron spectrometer using monochromatic Al-Kα radiation as the X-ray source. All the obtained spectra were calibrated to C 1s (264.8 eV) before analysis

Calculation of faradaic efficiency

The faradaic efficiency of the NORR in EFeMC designed electrolyte is defined as the amount of electric charge used for the target products (ammonium and hydroxylammonium) divided by the total charge that passed through the electrodes during the electrolysis. The concentrations of ammonium and hydroxylammonium ions were measured by ion chromatography. The FE for a specific product was calculated using the following equation:

$$FE\ (\%) = \frac{nF}{Q}\ x\ C\ \ x\ V\ \ x\ 100$$

where n is the electron number (e^-), F is the Faradaic constant (96,485.34 C/mole e^-), C is the product concentration (M), V is the electrolyte volume (L), and Q is the total charge passed (C).

In our experiments, we considered that five and three electrons are consumed to generate one NH_3 (or NH_4^+) and one NH_2OH (NH_3OH^+) molecule from the reduction of NO, respectively.

The rates of product formation (v) were calculated as follows:

$$v = \frac{(C \ x \ V)}{(t \ x \ A)}$$

where t is the reaction time (h) and A is the electrode area (m^2).

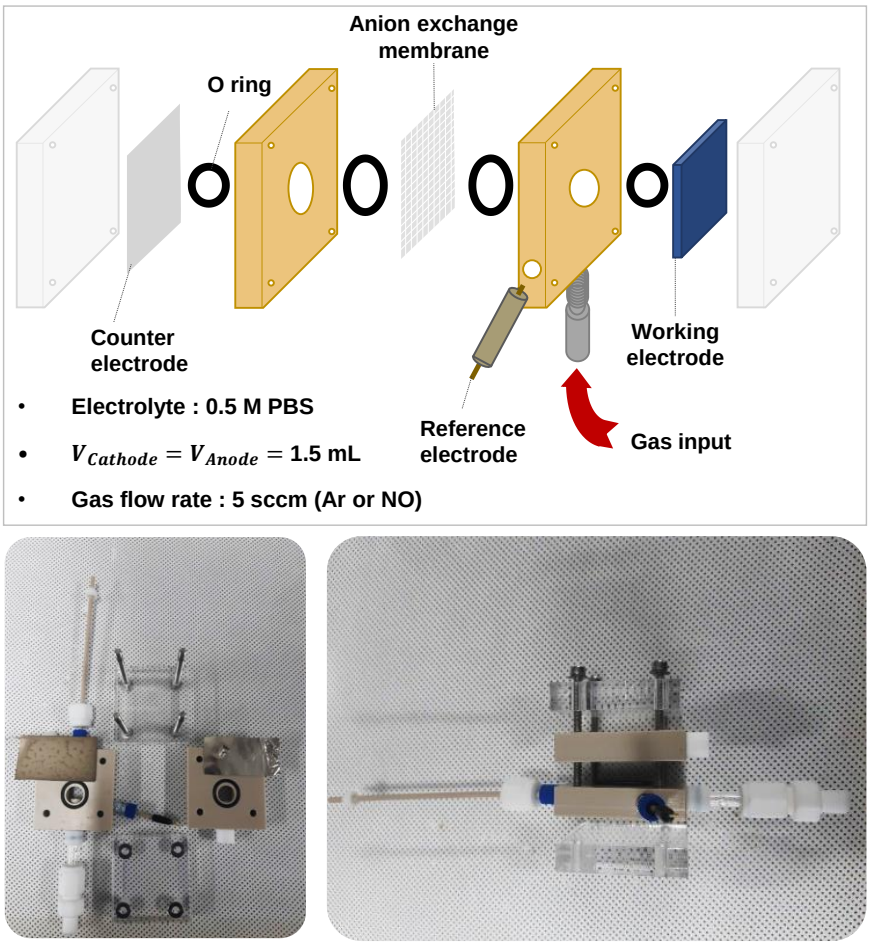

Figure S1. Schematic representation of an H-type cell configuration and its digital photographs showing each compartment.

Components of the electrolysis cell used for NORR in this study.

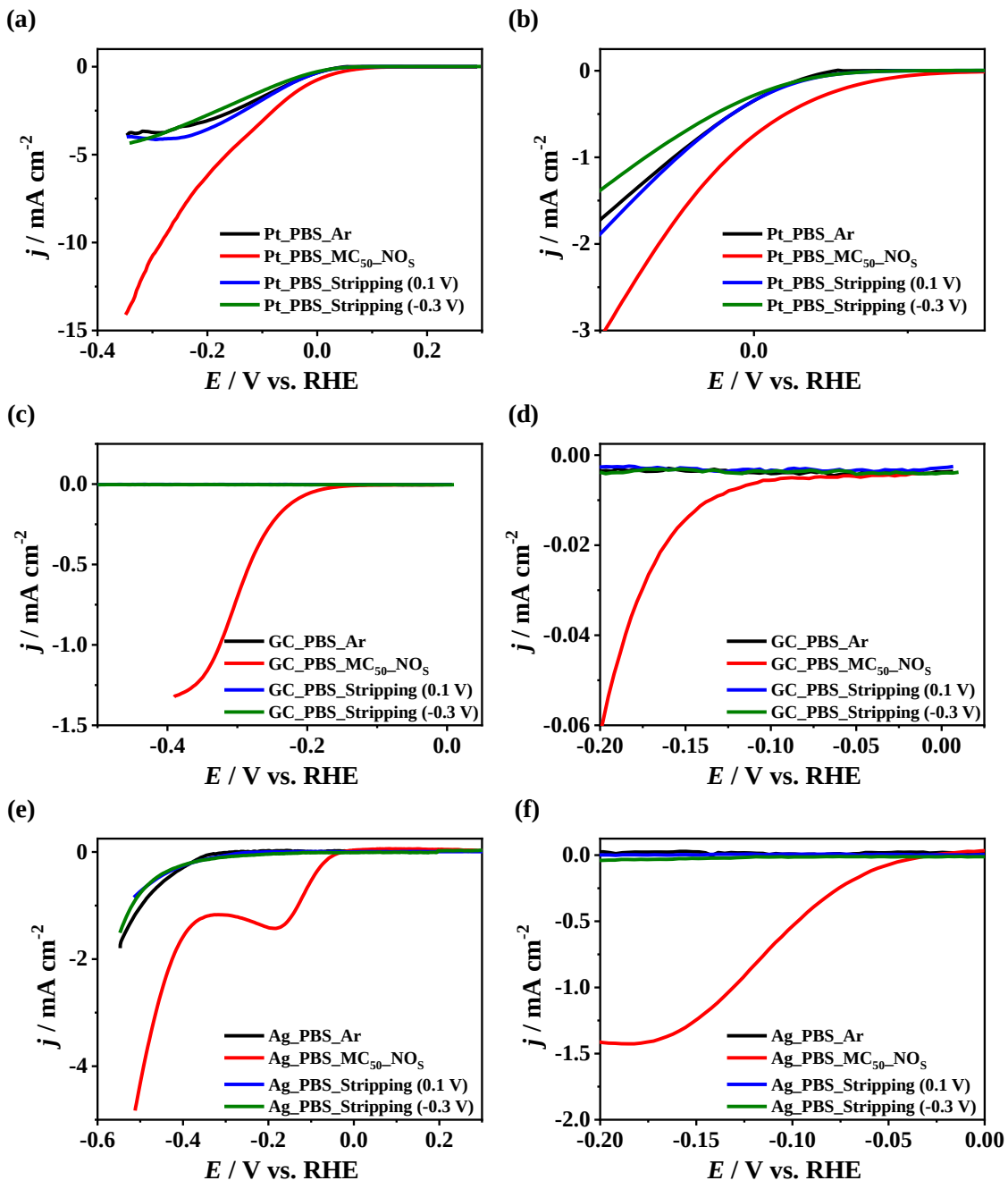

Figure S2. Electrochemical reductive desorption characteristics (stripping) of adsorbed NO@EFeMC species on cathode materials

Stripping tests of NO@EFeMC adsorbates on the surface of (a) Pt, (c) GC, and (e) Ag electrodes and (b, d, and f) corresponding magnified graphs of Pt, GC and Ag, respectively in PBS. (Potentials +0.1 V and -0.3 V were used for the adsorption of NO@EFeMC species on cathode material by chronoamperometry).

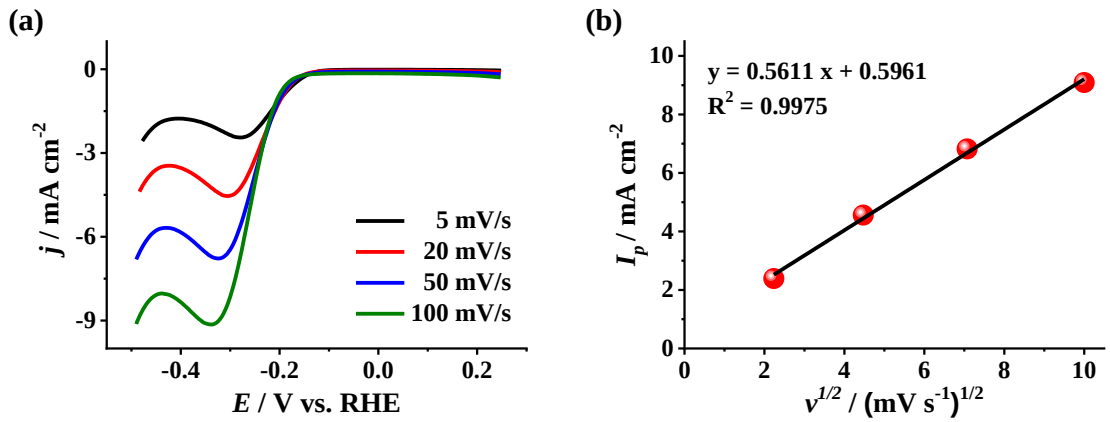

Figure S3. Effect of scan rates on the electrochemical behavior of NO@EFeMC species on Ag electrode in NO saturated designed electrolyte.

(a) Linear sweep voltammograms obtained at scan rates of 5, 20, 50, and 100 mV s^{-1} in PBS-MC_{50}-NO_s electrolyte.

(b) Plot showing linear dependence of I_p with $v^{1/2}$ and, where v is scan rate and I_p is cathodic peak current.

Randles-Sevcik equation:

$$I_{peak} = 0.4463\ \mathrm{nFAC}\left(\frac{\mathrm{nFvD}}{\mathrm{RT}}\right)^{\frac{1}{2}}$$

where, n is the number of electrons transferred, F is Faraday constant, A is the active surface area of electrode, D is the diffusion coefficient, C is the concentration, v is the scan rate, R is gas constant and T is the temperature.

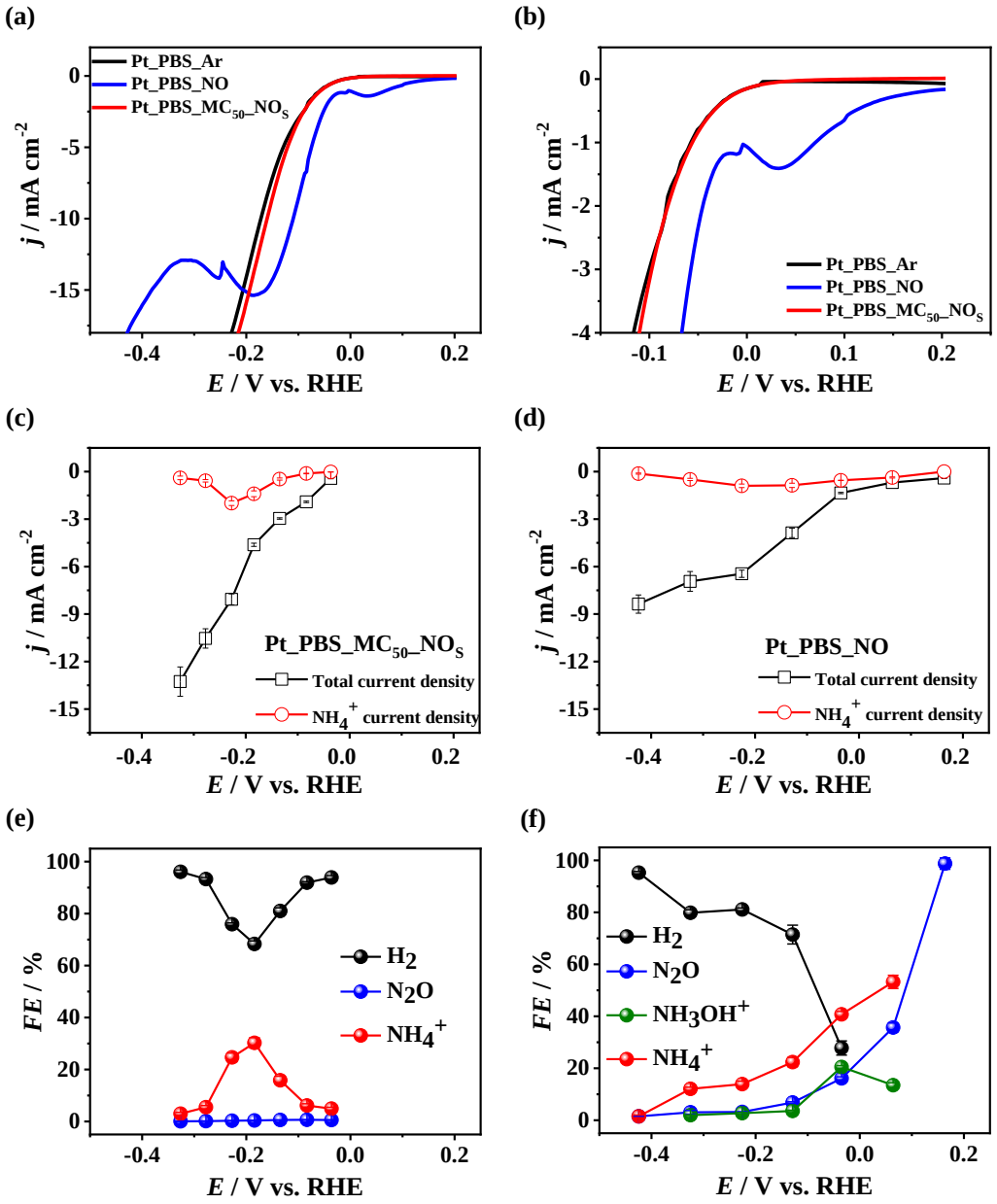

Figure S4. NORR on Pt electrode in PBS-MC$_{50}$-NO$_s$ electrolyte and in blank electrolyte (PBS solution without EFeMC additive).

(a) Linear sweep voltammograms and (b) their magnified plot for Pt electrode in PBS-MC$_{50}$-NO$_s$ electrolyte and in PBS at a constant flow of NO gas.

(c, d) Total and NH_4^+ partial current densities obtained after chronoamperometry on Pt electrode in PBS-MC$_{50}$-NO$_s$ electrolyte (c) and PBS at a constant flow of NO gas (d).

(e, f) Calculated faradaic efficiencies for the formation of gaseous and liquid products on Pt electrode in PBS-MC$_{50}$-NO$_s$ electrolyte (e) and in PBS at a constant flow of NO gas (f).

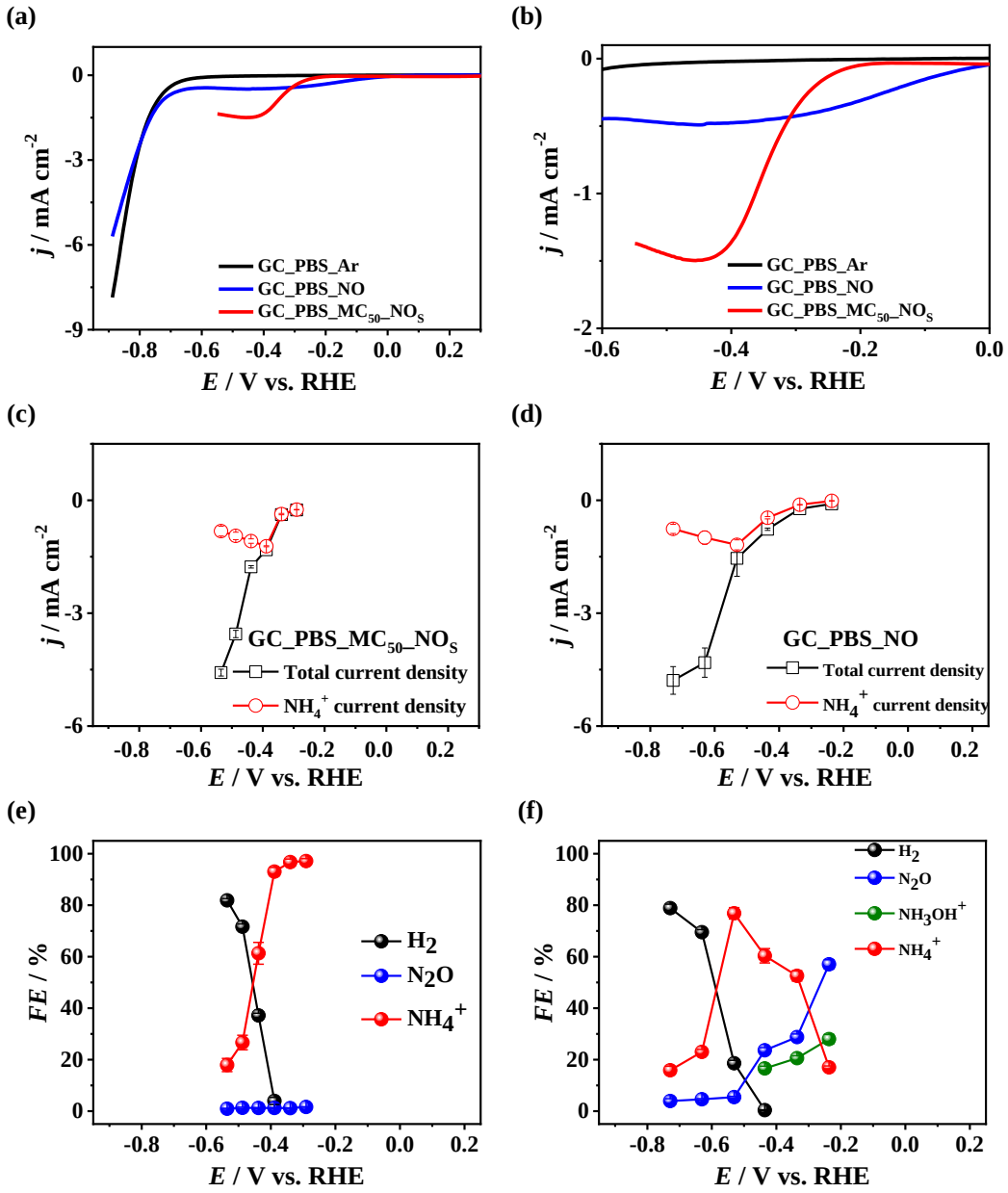

Figure S5. NORR on GC electrode in PBS-MC_{50}-NO_s electrolyte and in blank electrolyte (PBS solution without EFeMC additive).

(a) Linear sweep voltammograms and (b) their magnified plot for GC electrode in PBS-MC_{50}-NO_s electrolyte and in PBS at a constant flow of NO gas.

(c, d) Total and NH_4^+ partial current densities obtained after chronoamperometry on GC electrode in PBS-MC_{50}-NO_s electrolyte (c) and PBS at a constant flow of NO gas (d).

(e, f) Calculated faradaic efficiencies for the formation of gaseous and liquid products on GC electrode in PBS-MC_{50}-NO_s electrolyte (e) and in PBS at a constant flow of NO gas (f).

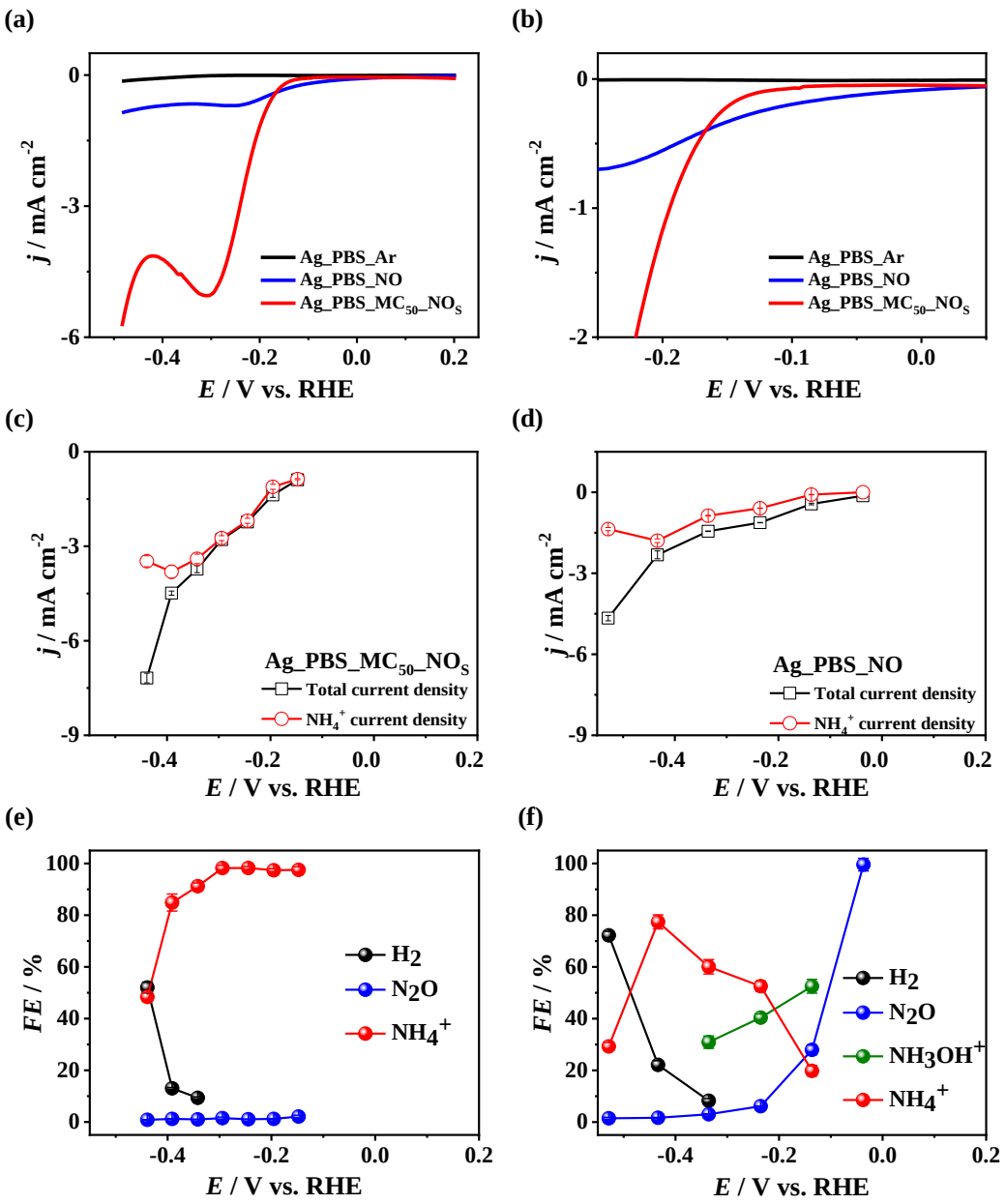

Figure S6. NORR on Ag electrode in PBS-MC$_{50}$-NO$_s$ electrolyte and in blank electrolyte (PBS solution without EFeMC additive).

(a) Linear sweep voltammograms and (b) their magnified plot for Ag electrode in PBS-MC$_{50}$-NO$_s$ electrolyte and in PBS at a constant flow of NO gas.

(c, d) Total and NH_4^+ partial current densities obtained after chronoamperometry on Ag electrode in PBS-MC$_{50}$-NO$_s$ electrolyte (c) and PBS at a constant flow of NO gas (d).

(e, f) Calculated faradaic efficiencies for the formation of gaseous and liquid products on Ag electrode in PBS-MC$_{50}$-NO$_s$ electrolyte (e) and in PBS at a constant flow of NO gas (F).

NORR Product Analysis

The gaseous products (N_2O, N_2, and H_2) generated in the cathodic chamber were delivered into an online gas chromatograph (iGC7200, DS Science) equipped with a HP-PLOT 5A column coupled with a pulsed discharge detector as shown in Figure S7. A typical gas chromatograph and the calibration curves were shown in Figure S8. The liquid products (NH_3OH^+ and NH_4^+) were quantified using an ion chromatograph (883 Basic IC Plus, Metrohm) equipped with chemical suppression and a conductimetric detector. The ion chromatograph was equipped with a Metrosep C6 column (150 mm × 4 mm) at 30°C with a mobile phase composed of 1.7 mM nitric acid and 1.7 mM dipicolinic acid as an eluent at a flow rate of 0.9 mL min^{-1}. The typical ion chromatographs of NH_3OH^+ and NH_4^+ and their corresponding calibration curves are shown in Figure S9.

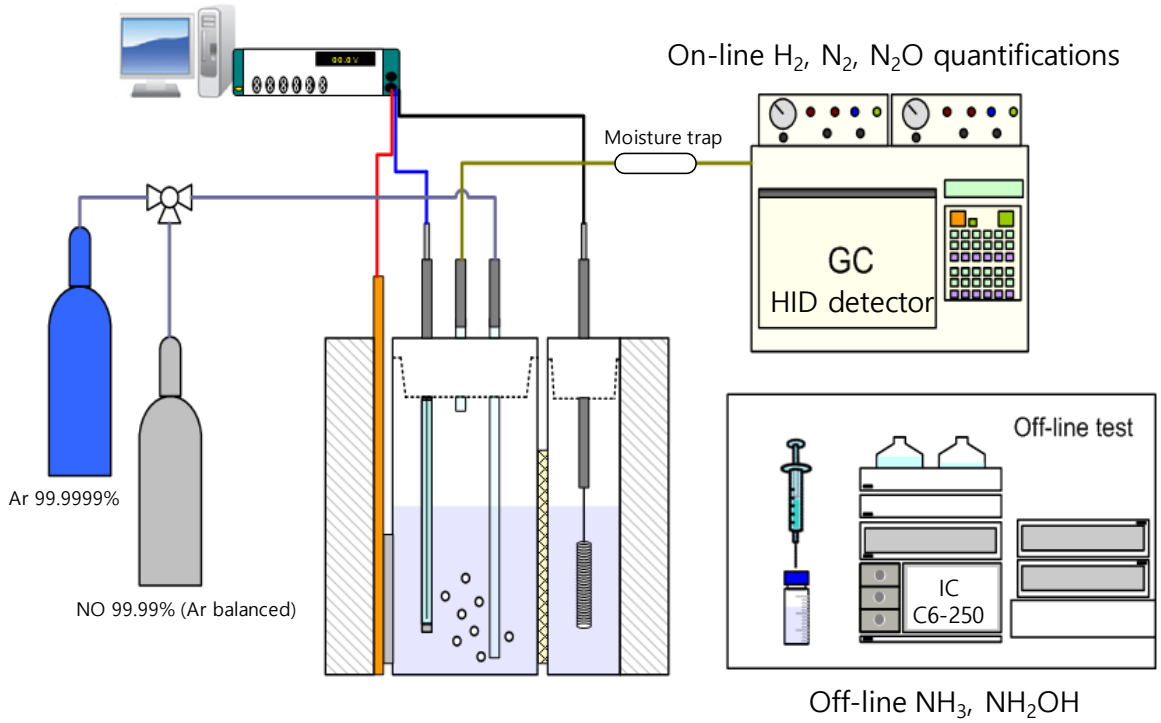

Figure S7. Schematic diagram of the online analytical system for the analysis of gaseous and liquid products of the electrochemical NO reduction reaction.

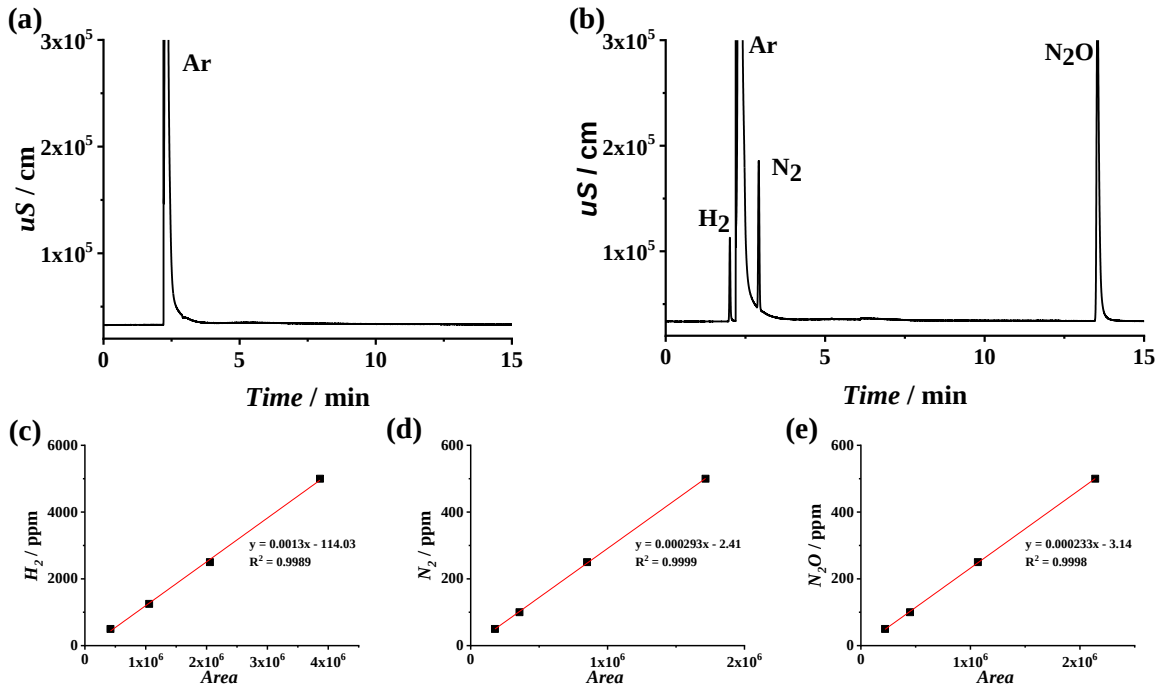

Figure S8. Gas chromatographic analysis of the gaseous products of NORR.

(a) Blank chromatogram of Ar flow.

(b) Gaseous products generated from NORR on Ag electrode in blank electrolyte (PBS solution) at -0.40 V_{RHE}.

(c, d, e) Calibration curves for the quantification of H_2 (c), N_2 (d) and N_2O (e).

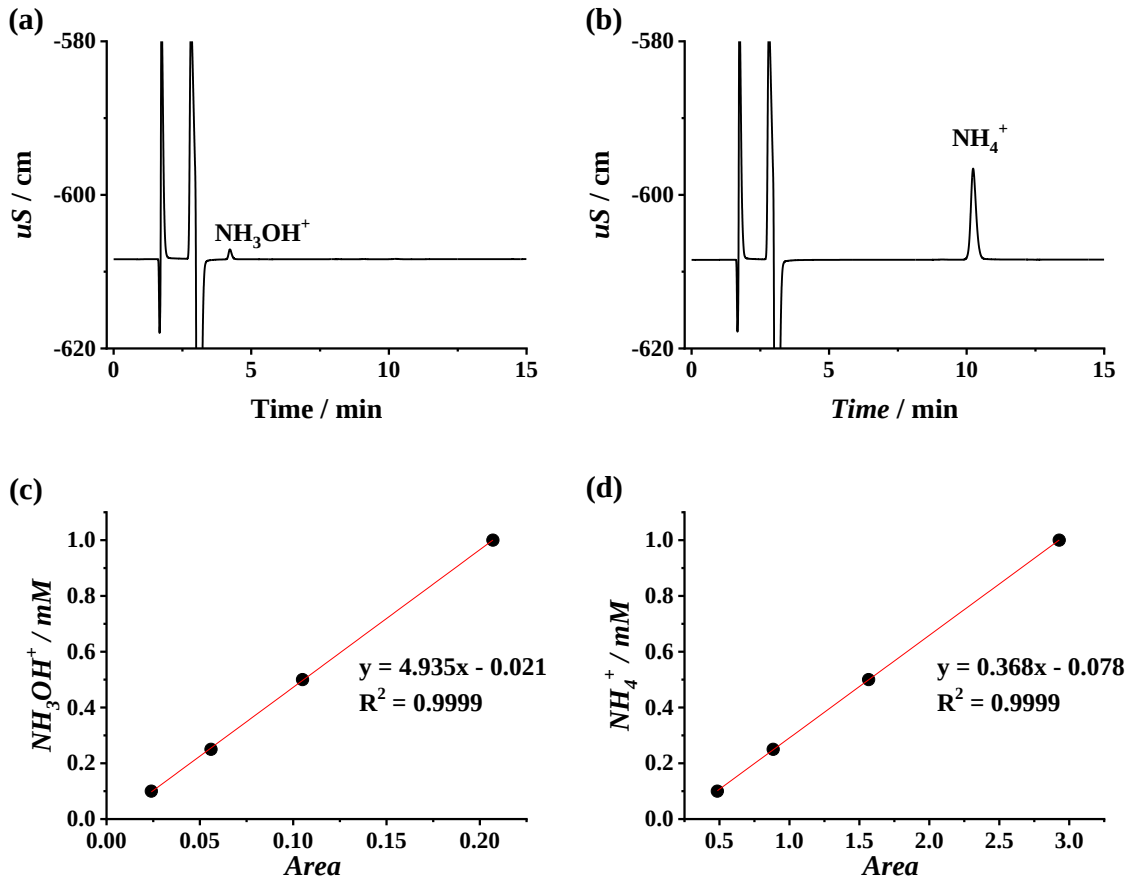

Figure S9. Ion chromatographic analysis of the liquid products of NORR.

(a, b) Liquid products generated from NORR on Ag electrode in blank electrolyte (PBS solution) at -0.40 V_{RHE} for 1 h.

(c, d) Calibration curves for NH_3OH^+ (c) and NH_4^+ (d).

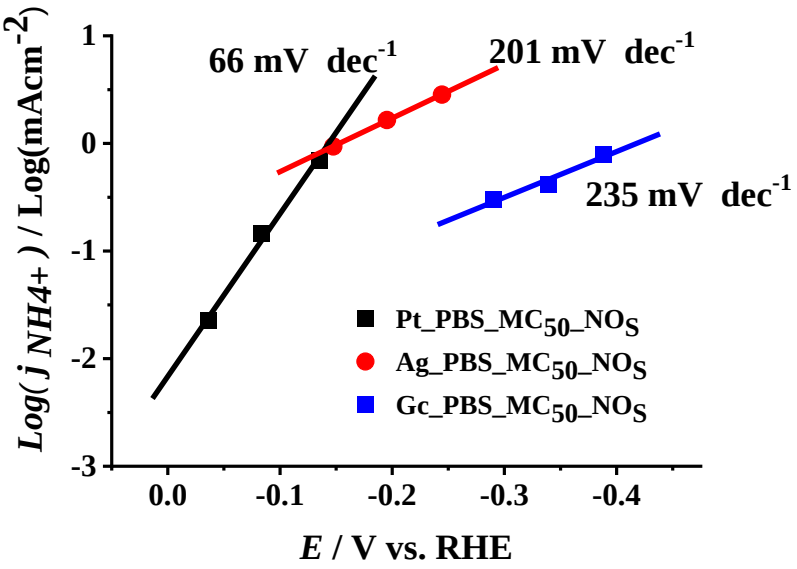

Figure S10. Tafel plots of Pt, GC and Ag electrodes in PBS-MC_{50}-NO_s electrolyte for partial NH_4^+ current densities.

Electrochemical impedance spectroscopy (EIS)

EIS analysis was studied by using the Nyquist plot to investigate electron transfer process and electrical conductivity of the electrodes. The Nyquist plots of NORR for prepared electrodes (GC, Pt, Ag and Agn) were obtained at -0.3 V_{RHE} in the range of 1 MHz to 1 Hz in PBS-MC50-NOS electrolyte. R_{ct} is related to the number of electrons transferred from the catalyst surface to the reactant as well as the intermediate formation inside the double layer.[2] The Nyquist plot obtained from Agn electrode is shown in **Figure S20**.

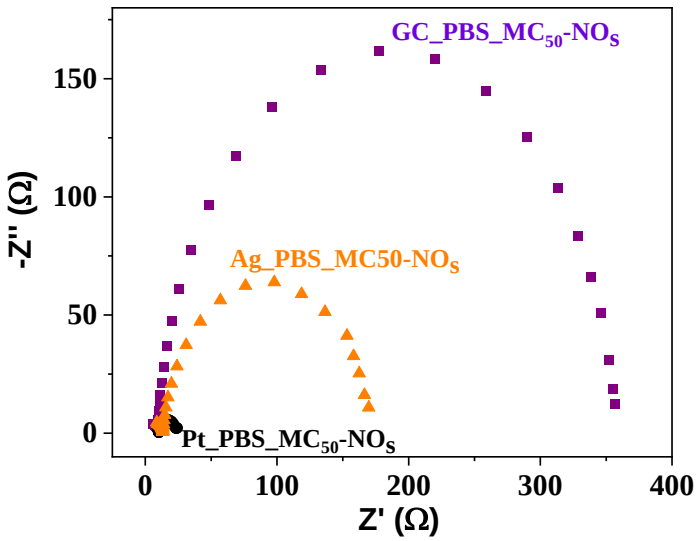

Figure S11. Electrochemical impedance spectroscopy analysis of NORR on Pt, GC and Ag electrodes at -0.3 V_{RHE}.

Full conversion experiment

In order to confirm the stoichiometric correlation between EFeMC and NO, full conversion experimental was performed. NO@EFeMC was prepared by purging 1% NO in an aqueous solution containing 50 mM EFeMC, and then electrochemically reduced on Ag electrode for a long enough time to be completely converted to NH_4^+. As a result, the NH_4^+ concentration is 49 mM, which is consistent with that of initial EFeMC.

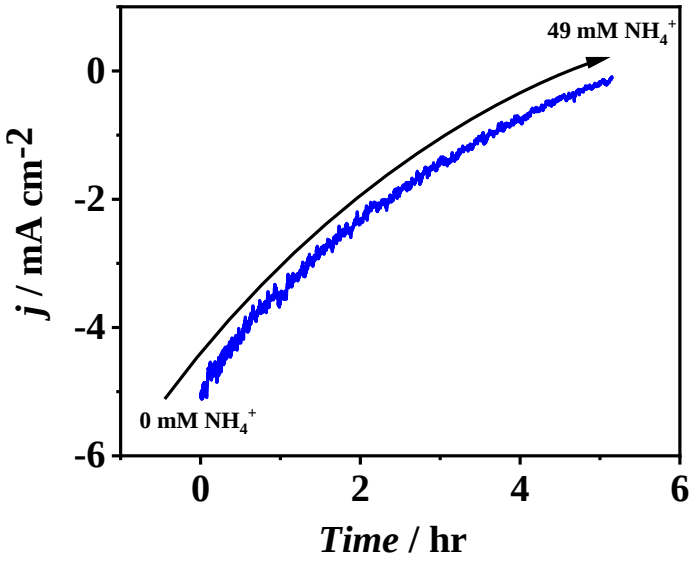

Figure S12. Full conversion experiment on Ag electrode with PBS-MC_{50}-NO_S

Computational analysis by using DFT for NORR on Ag electrode

To model the NO reduction reaction on Ag electrode, we performed density functional theory (DFT) calculations using the Vienna Ab-initio Software Package (VASP) program with the choice of Perdew-Burke-Emzerhof (PBE) exchange-correlation functional.[3,4] The electron-ion interaction was described using the projector-augmented-wave (PAW) scheme. We first optimized the bulk structures of Ag using an energy cutoff of 650 eV and Monkhorst-pack (11×11×11) k-point mesh. We considered the close-packed surface of (3×3) Ag (111) with 4 layers, and stepped surface of (3×1) Ag (211) with 6 layers, where the bottom two or three layers were fixed at their lattice sites for Ag (111) or Ag (211), respectively. We included an additional vacuum layer of 15 Å and applied a dipole correction along the surface normal direction. We set an energy cutoff of 500 eV and sampled the reciprocal spaces using a Γ-centered (6×6×1) k-point mesh for Ag (111), and Monkhorst-pack (6×6×1) k-point mesh for Ag (211). Using partial Hessian calculations for intermediate species, we included a finite temperature correction including the zero-point energy using harmonic oscillator partition function, and for gas molecular species, translational and rotational free energies were included.

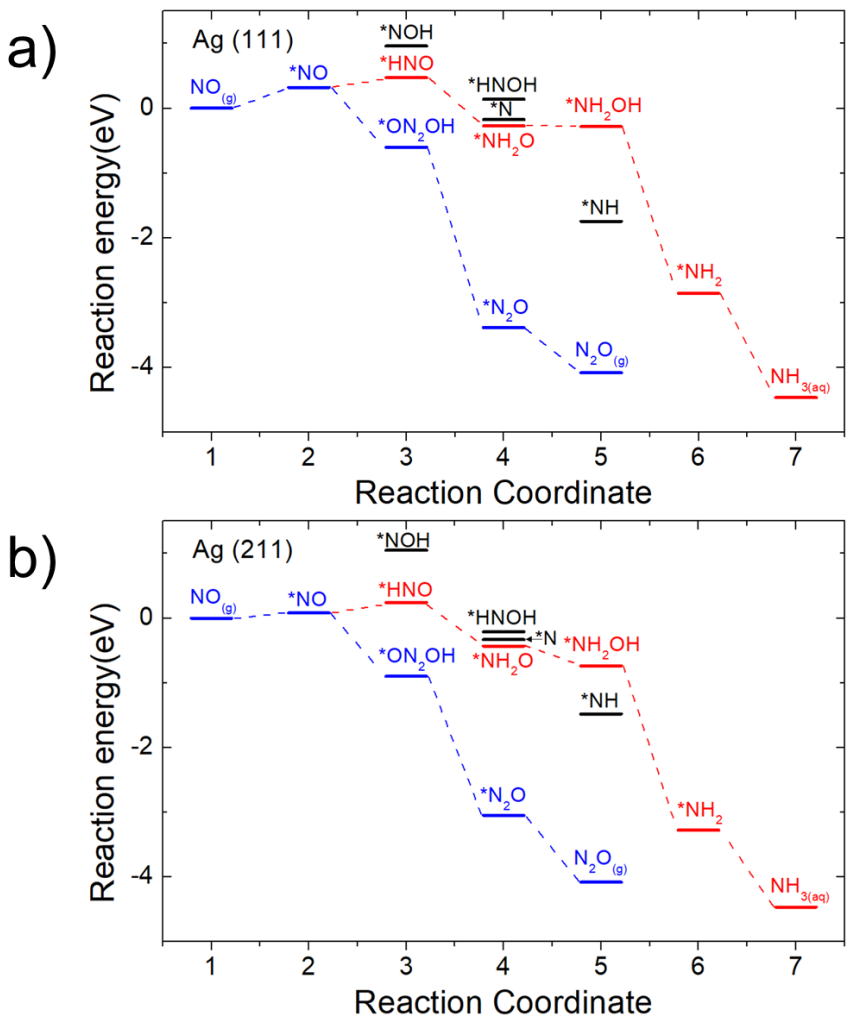

Figure S13. Free energies of reactions calculated using DFT for NO reduction on a) Ag (111) and b) Ag (211) surface. NO reduction free energies for N_2O production (blue) and NH_3 production (red) are shown at 0 V_{RHE}.

Investigation of chemical and electrochemical interactions between hydroxylamine (NH_3OH^+) species and metal chelating agent, EFeMC.

Based on the results of the chemical and electrochemical interactions shown in Figures S12 and S13, we hypothesized two possible scenarios that could occur during the conversion process. In the first scenario, the applied potential may have reduced the activation energy required for the chemical reaction between the NH_3OH^+ and EFeMC. In this case, free standing NH_3OH^+ species must be able to collide with two other EFeMC species for the redox reaction to proceed, and the thermodynamic potential at which the reaction between NH_3OH^+ and EFeMC takes place must be more positive than 0.26 V_{RHE} so that the reverse reaction does not occur. In the second scenario, the applied potential may have induced the formation of NH_3OH^+@EFeMC - complexes. In this case, reduction may proceed spontaneously through a proton-coupled electron transfer process if each step in the reaction afterward is favorable.

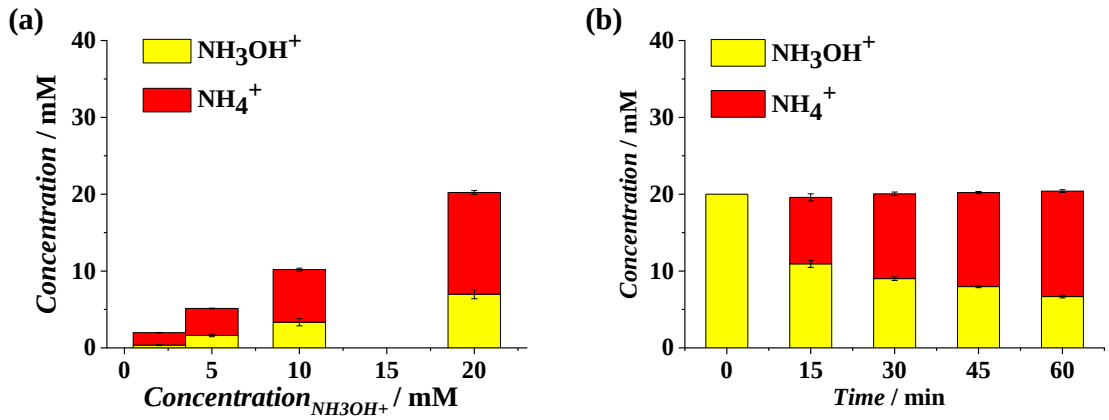

Figure S14. Chemical interaction of hydroxylamine (NH_3OH^+) with EFeMC.

(A) Effect of initial NH_3OH^+ concentration (2, 5, 10, and 20 mM) on the conversion of NH_3OH^+ to NH_4^+ after 1 h reaction.

(B) Effect of reaction time on the conversion of 20 mM NH_3OH^+ to NH_4^+.

Table S1. Possible chemical and electrochemical reactions during EFeMC-NORR

$2\ NH_2OH + 4\ Fe^{III} \rightarrow N_2O + 4\ Fe^{II} + 4\ H^+ + H_2O$
$NH_2OH + 2\ Fe^{II} + 2\ H^+ \rightarrow NH_3 + 2\ Fe^{III} + H_2O$
$NO\ (aq) + NO\ (ads) + 2\ e^- + 2\ H^+ \rightarrow N_2O + H_2O$

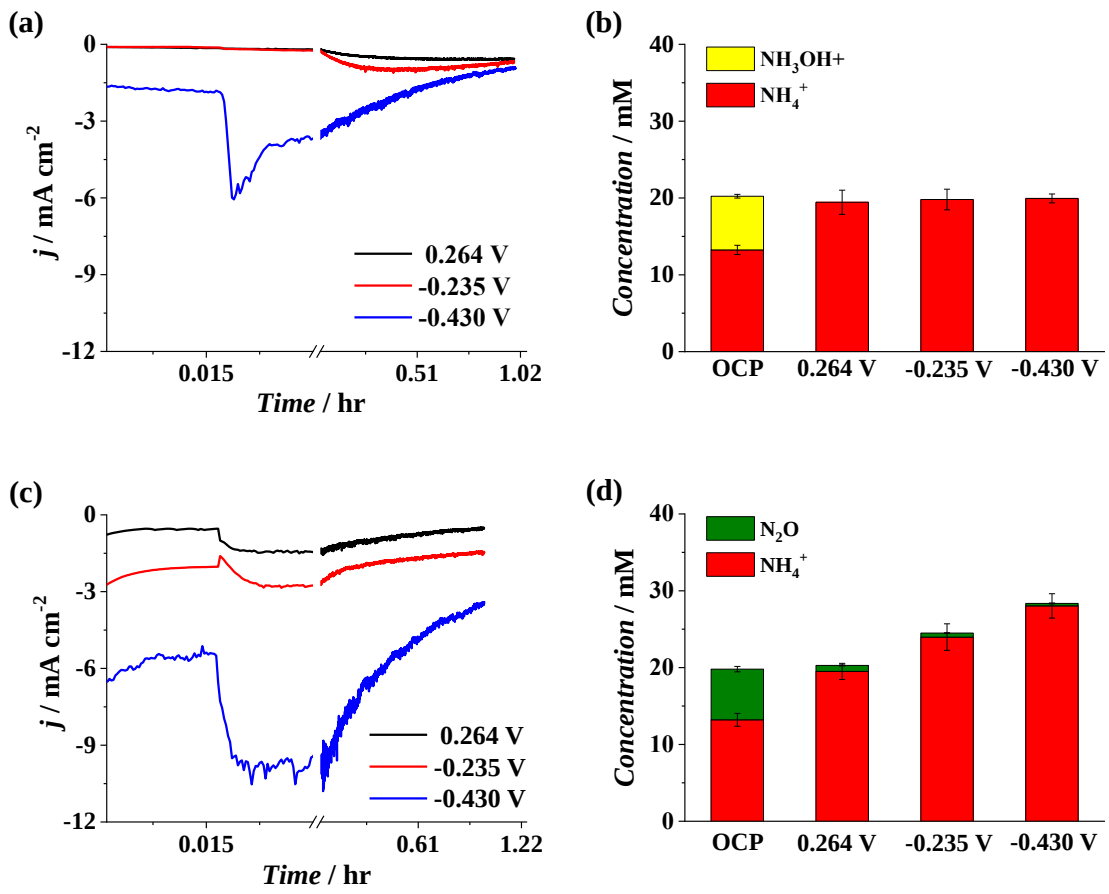

Figure S15. Electrochemical interaction of hydroxylamine with EFeMC species and NO@EFeMC species.

(a) Chronoamperometry curves of Ag electrode in PBS-MC_{50} with the addition of 20 mM NH_2OH at 0.015 h.

(b) Concentrations of final products after 1 h chronoamperometry on Ag electrode in PBS-MC_{50}.

(c) Chronoamperometry curves of Ag electrode in PBS-MC_{50}-NO_s electrolyte with the addition of 20 mM NH_2OH at 0.015 h.

(d) Concentrations of final products after 1 h chronoamperometry on Ag electrode in PBS-MC_{50}-NO_s electrolyte.

Computational analysis by using DFT for EFeMC and reaction intermediates

We performed the density functional theory (DFT) calculations using the Jaguar 8.4 software package with a choice of Minnesota 2006 functional (M06) for EFeMC and reaction intermediates[5] and the LACVP**++ basis set, which employs the LANL2DZ effective core basis set, for Fe and Ag, while other elements were described with the standard Pople's 6-31G**++ basis set.[6] The Gibbs free energy values at 1 atm and 298.15 K were estimated by calculating the vibrational frequencies, and the solvation free energies were calculated using the Poisson–Boltzmann implicit solvation model, where the dielectric constant and probe radius were set as 80.37 and 1.40 Å, respectively, as implemented in the Jaguar 8.4 package.

To compute the free energy changes during the electrochemical reactions, the computational hydrogen electrode (CHE) was employed, which yielded the chemical potentials of a proton and an electron as $\mu[H^+] + \mu[e^-] = 1/2\mu[H_{2(g)}] - eU = (-15.93 - eU)$ eV[7], where U denotes the bias potential versus RHE. The chemical potential of the electron was set as $\mu[e^-] = (-4.44 - eU)$ eV, yielding $\mu[H^+] = -11.49$ eV (cf. experimental solvation free energy of a proton ranges from −10.95 eV to −11.92 eV).[8] The binding energy of A@EFeMC (A=intermediate) on AgNP was calculated using the reaction energy of the following reaction;

$$A@EFeMC + Ag_{13} \rightarrow Ag_{13}\text{-}A@EFeMC$$

A=NO case, as an example, is graphically shown in **Figure S16**.

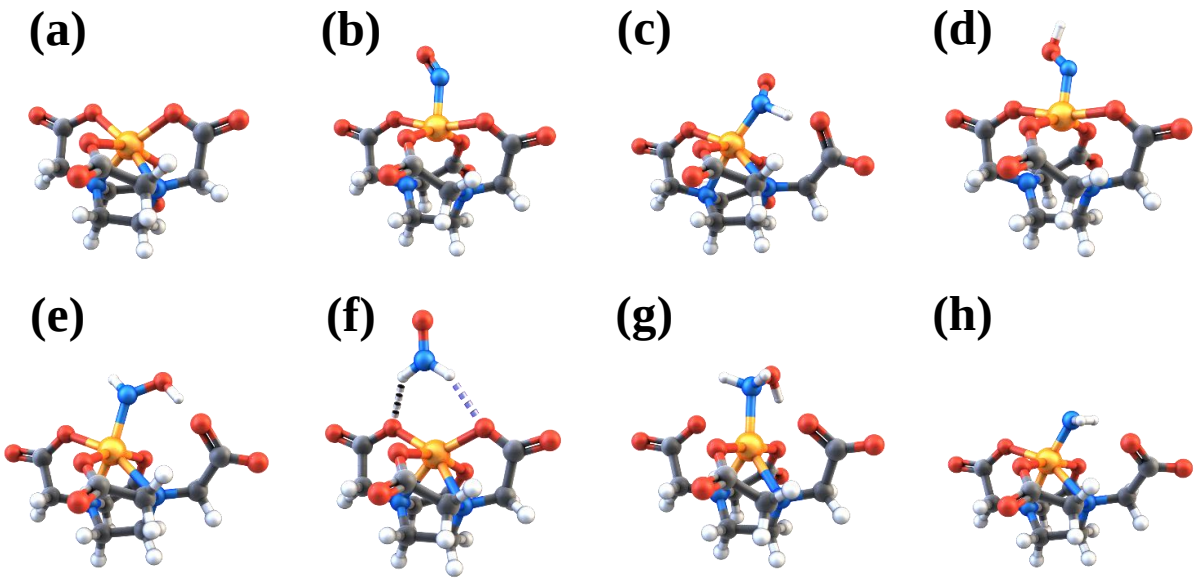

Figure S16. DFT calculation based optimized structures of reaction intermediate-EFeMC complexes.

Atomic structures of (a) free EFeMC [=*(II)], (b) *(II)-NO, (c) *(II)-HNO, (d) *(II)-NOH, (e) *(II)-NHOH, (f) *(II)-NH_2O, (g) *(II)-NH_2OH, and (h) *(II)-NH_2.

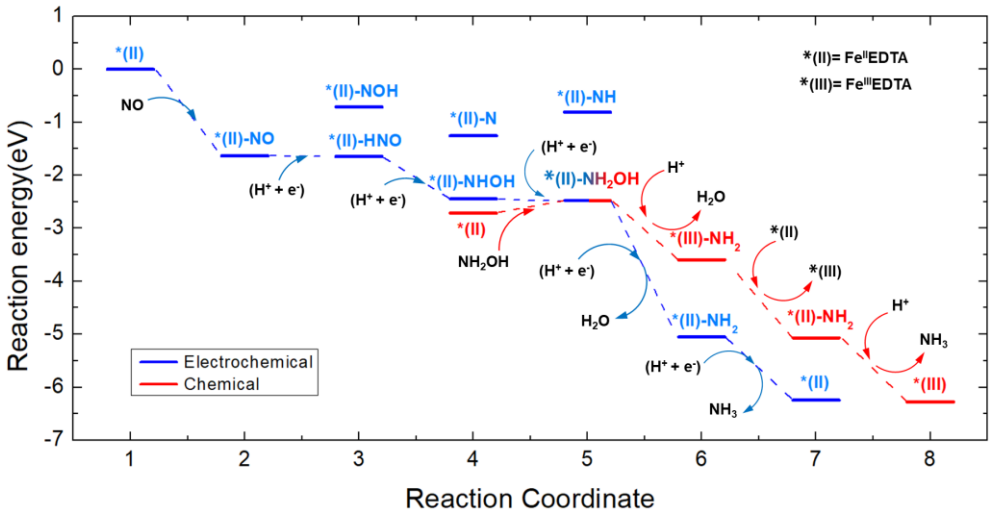

Figure S17. Free energies of reactions calculated using DFT for electrochemical (blue) and chemical (red) pathways of hydroxylamine reduction.

Reaction free energies for the electrochemical pathway via HNO and NOH pathways are shown at -0.34 V_{RHE}.

For the chemical pathway, Fe^{2+} species in EFeMC is assumed to be oxidized into Fe^{3+} species.

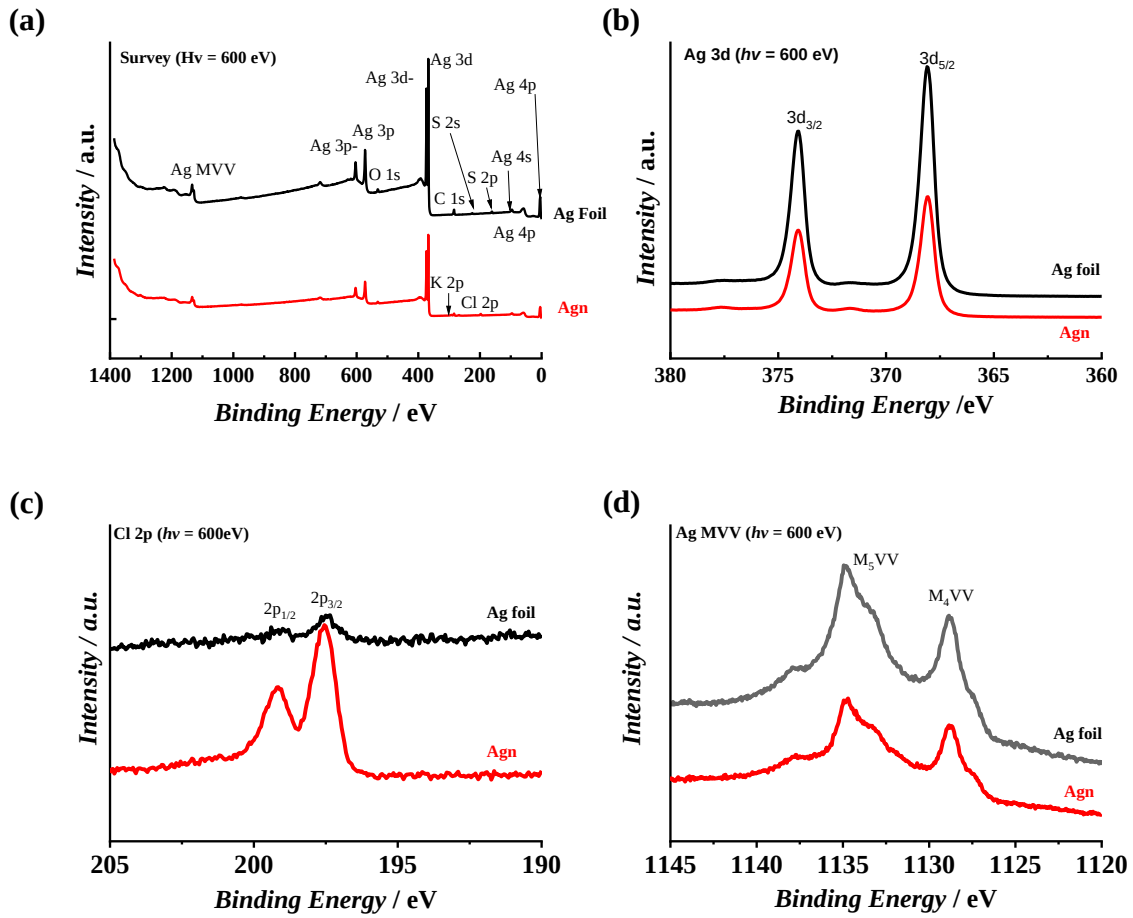

Figure 18. X-ray photoelectron spectra of Ag foil (black) and Agn (red).

X-ray photoelectron spectra (a) Survey scan, (b) Ag 3d, (c) Cl 2p (d) Ag MVV of Ag foil (black) and Agn (red).

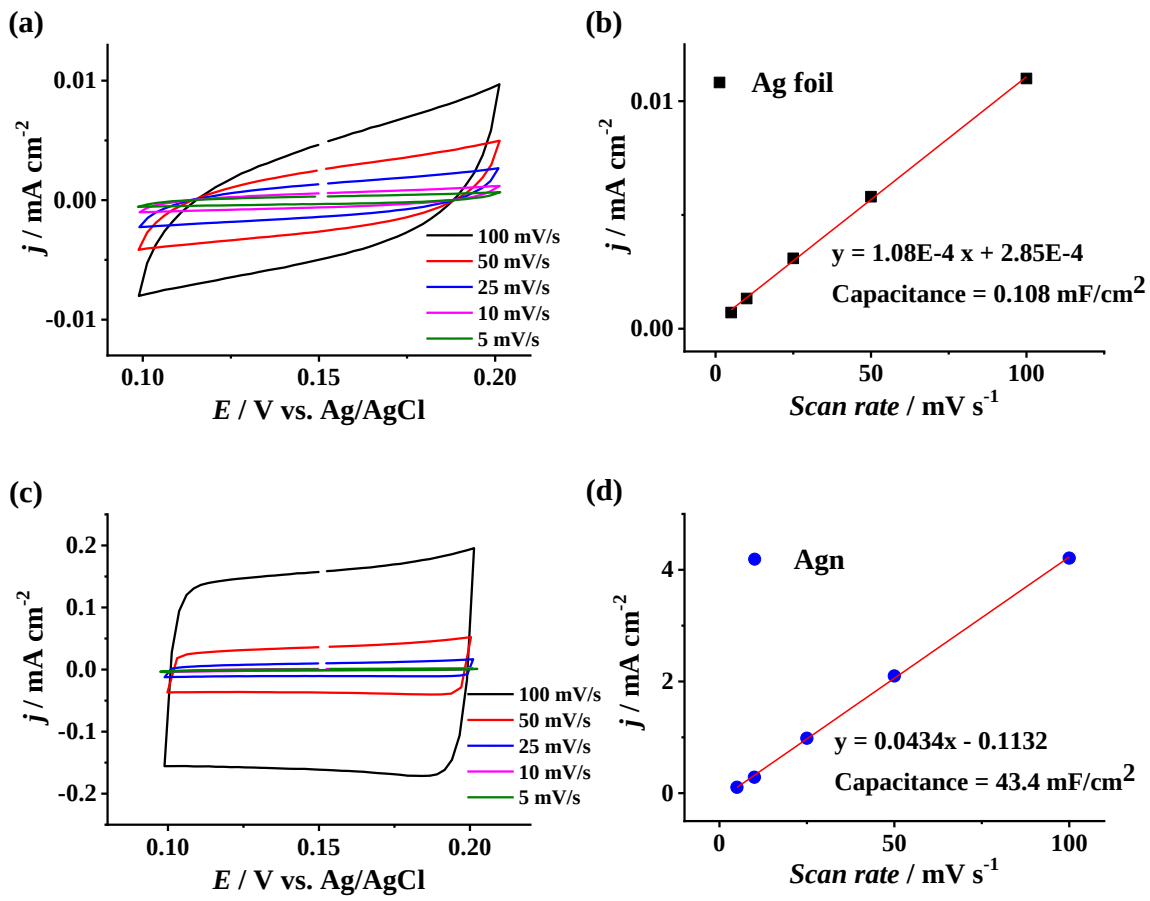

Figure S19. Electrochemical capacitance measurement.

(a) Cyclic voltammetry profiles for Ag electrode in the non-Faradaic potential region

(b) The calculated capacitances of Ag electrode from the current density vs. scan rate relationship.

(c) Cyclic voltammetry profiles for nanostructured Ag in the non-Faradaic potential region

(d) The calculated capacitances of nanostructured Ag electrodes from the current density vs. scan rate relationship.

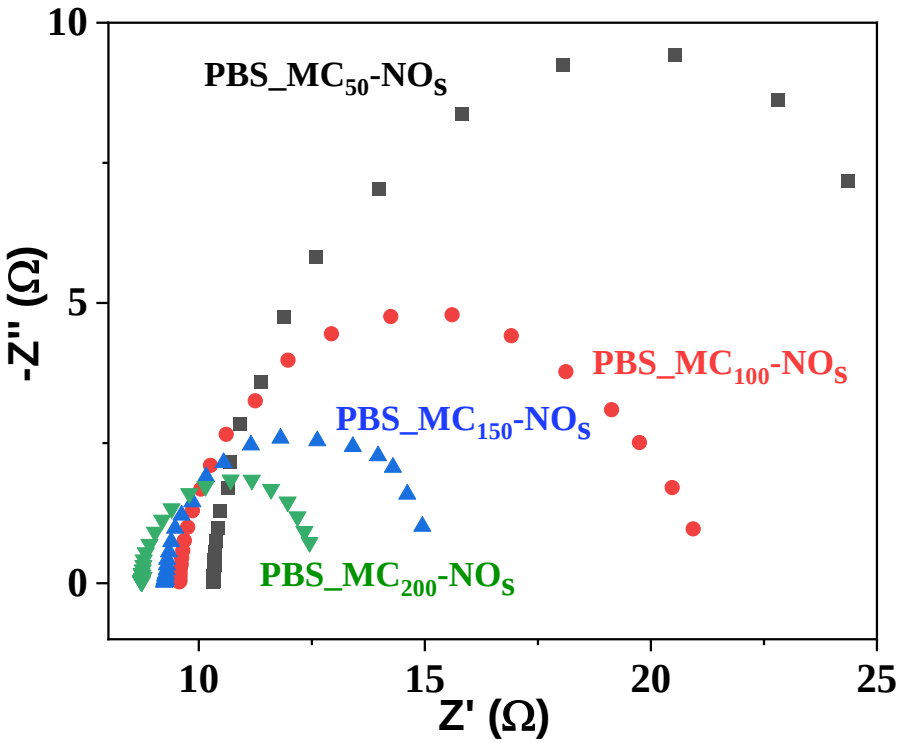

Figure S20. Electrochemical impedance spectroscopy analysis of NORR on Agn electrodes at -0.3 V_{RHE} with different concentrations of EFeMC.

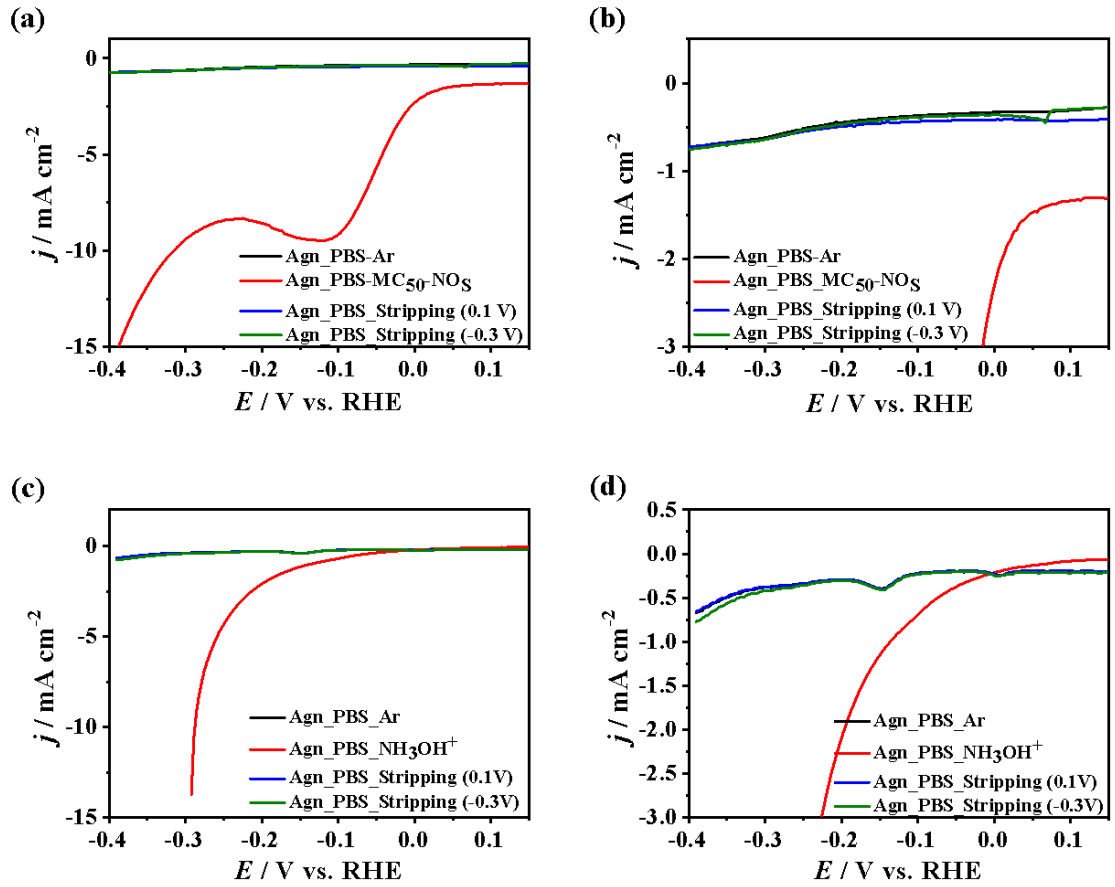

Figure S21. Electrochemical reduction of (a) NO@MC species and (c) NH_3OH^+ adlayer on Agn electrode and (b and d) the magnified graphs.

The adsorption occurred through 1 min chronoamperometry at +0.1 V and -0.3 V_{RHE} in an Ar-purged PBS-MC_{50}-NO_s solution or 50 mM NH_3OH^+ solution and the electrodes were then transferred to a blank electrolyte for stripping, which was performed at a scan rate of 20 mV s^{-1}.

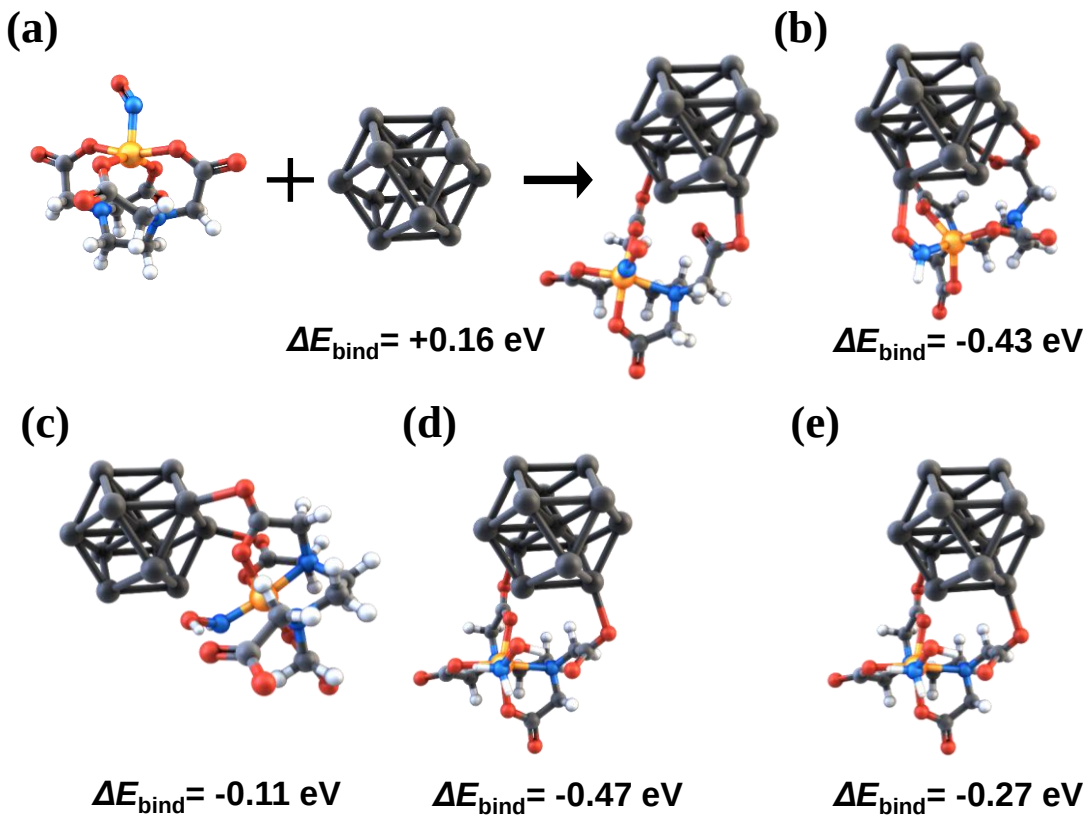

Figure S22. DFT calculation based optimized structures of reaction intermediate-EFeMC-Ag NP complexes.

(a) Atomic structures of 13-atom silver nanoparticle (AgNP) and *(II)-NO-AgNP. The binding energy (ΔE_{bind}) of AgNP with an intermediate@EFeMC complex is also shown (a more negative value implies stronger binding).

Atomic structures of (b) *(II)-HNO-AgNP, (c) *(II)-NHOH-AgNP, (d) *(II)-NH_2O-AgNP, and (e) *(II)-NH_2OH-AgNP.

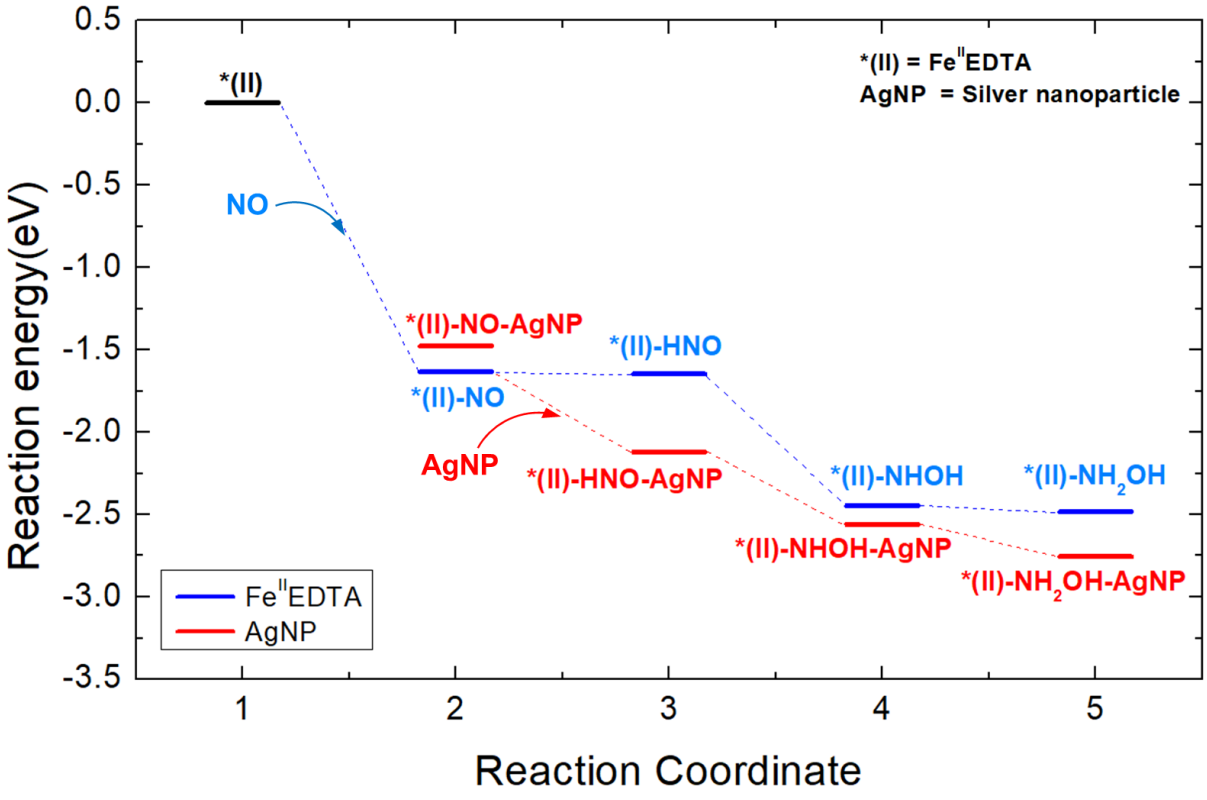

Figure S23. DFT based calculated free energies of reactions for the electrochemical reduction of NO to NH_2OH with Ag NP (red) and without Ag NP (blue).

Reaction free energies for the electrochemical pathway are shown at -0.34 V_{RHE}.

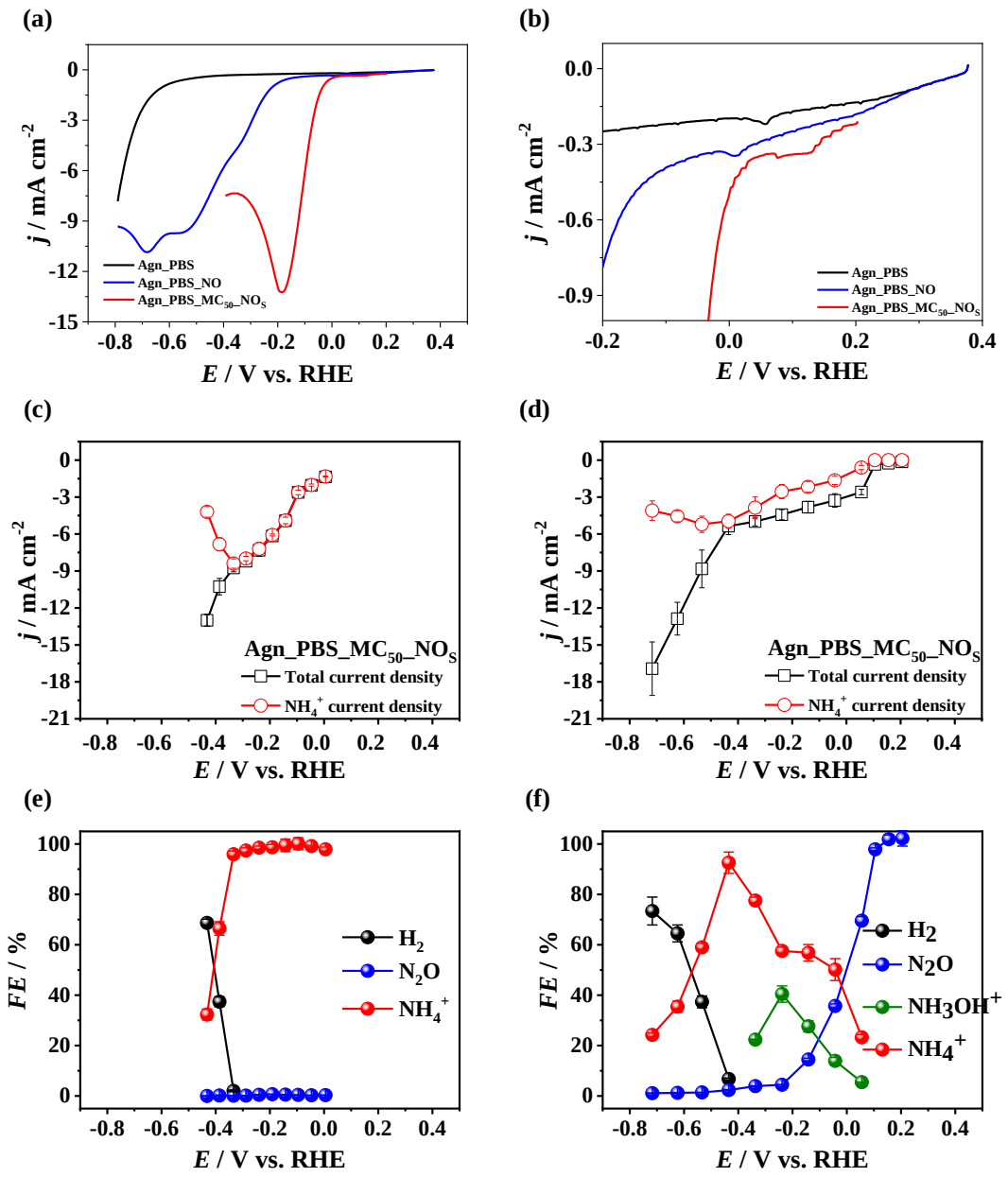

Figure S24. NORR on Agn electrode in PBS-MC$_{50}$-NO$_s$ electrolyte and in blank electrolyte (PBS solution without EFeMC additive).

(a) Linear sweep voltammograms and (b) their magnified plot for Agn electrode in PBS-MC$_{50}$-NO$_s$ electrolyte and PBS at a constant flow of NO gas.

(c, d) Total and NH_4^+ partial current densities obtained after chronoamperometry on Agn electrode in PBS-MC$_{50}$-NO$_s$ electrolyte (c) and PBS at a constant flow of NO gas (d).

(e, f) Calculated faradaic efficiencies for the formation of gaseous and liquid products on Agn electrode in PBS-MC$_{50}$-NO$_s$ electrolyte (e) and in PBS at a constant flow of NO gas (f).

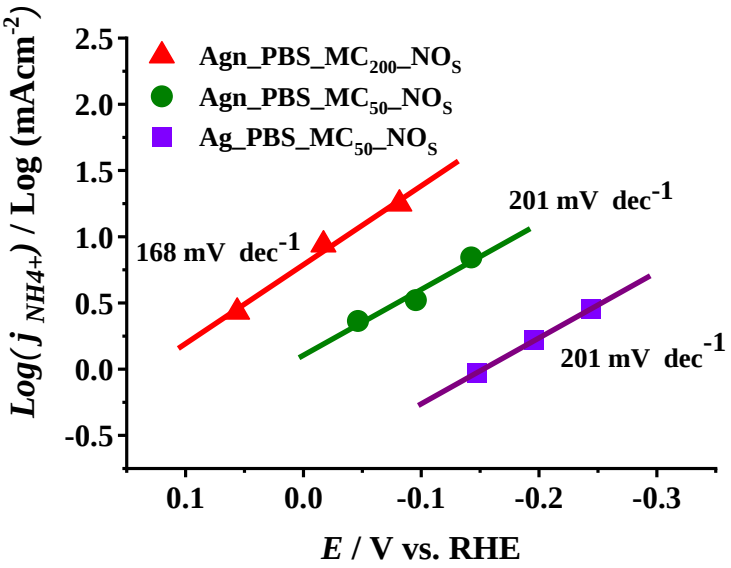

Figure S25. Tafel plots of Ag and Agn electrodes in PBS-MC$_x$-NO$_s$ electrolyte, (where x = 50 and 200 is the mM concentration of EFeMC in PBS) for partial NH_4^+ current densities.

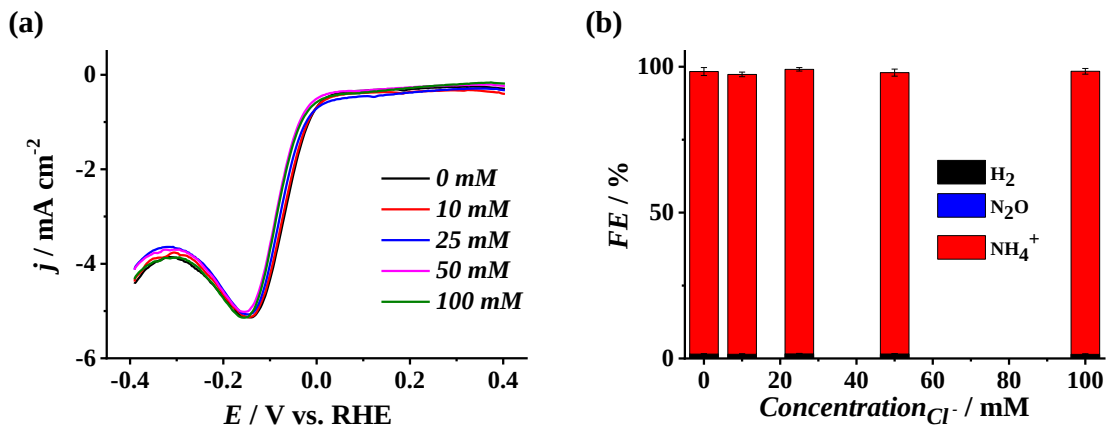

Figure S26. Effect of chloride ion on NORR on the Agn electrode in PBS-MC_{50}-NO_s electrolyte.

(a) Linear sweep voltammmograms on Agn electrode for NORR in PBS-MC_{50}-NO_s electrolyte in the presence of 0, 10, 25, 50 and 100 mM KCl.

(b) Faradaic efficiencies for the formation of gaseous and liquid products on Agn electrode in PBS-MC_{50}-NO_s electrolyte in the presence of 0, 10, 25, 50, and 100 mM KCl.

Isotope labeling experiments

^{15}NO was generated by introducing 5 M $Na^{15}NO_2$ (0.1 mL) in 1 M H_2SO_4 (100 mL) and captured in a gas sampling bag with Ar carrier gas at a flow rate of 20 mL/min for 50 min. The concentration of ^{15}NO was about 0.97% (9,700 ppm). Then ^{15}NO@EFeMC was prepared by purging ^{15}NO into the cathodic compartment of an electrochemical cell containing 200 mM EFeMC (1.5 mL) at a flow rate of 5 sccm for 3 h. After electrolysis, NMR samples were prepared by mixing 0.8 mL of the product solution and 0.2 mL of d6-DMSO. The solution pH was adjusted by using 4 M H_2SO_4 solution. The NMR spectra of the prepared sample was compared with that of $^{15}NH_4^+$ and $^{14}NH_4^+$ standards to clarify the source of ammonia. In addition to this, a series of $^{15}NH_4^+$ solution with known concentration of 5, 10, 15, 20 mM were prepared for quantification of $^{15}NH_4^+$ contained in prepared sample

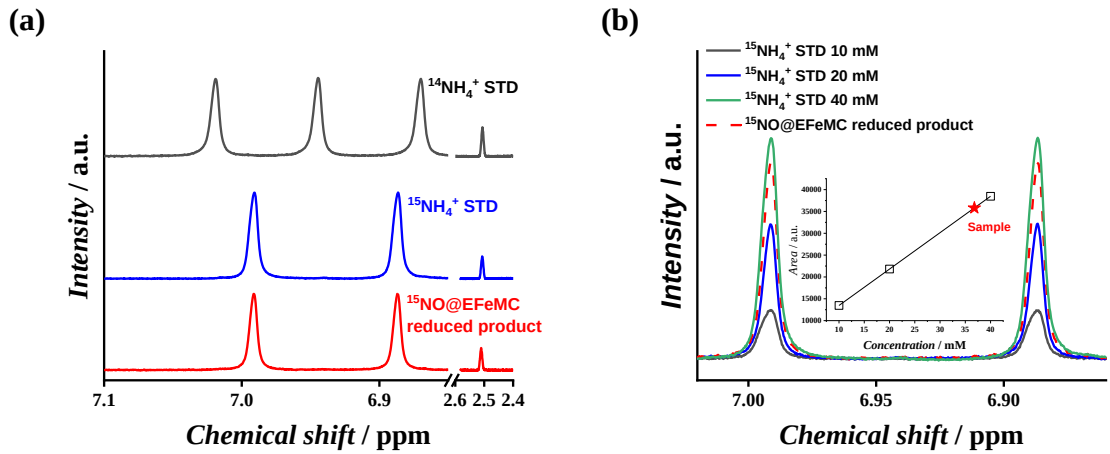

Figure S27. Isotope labeling experiment. ^{1}H-NMR spectra of 40 mM $^{14}NH_4^+$ standard, $^{15}NH_4^+$ standard and electrolyte obtained from electrolysis of 40 mM ^{15}NO@EFeMC (a) and ^{1}H-NMR spectra of $^{15}NH_4^+$ standard 10, 20, 40 mM and calibration curve (inserted) for quantification (b).

Long term experiment in PBS-MC_{200}-NO_s electrolyte

Long term experiment on nanostructured Ag was performed in a flow cell system by circulating electrolyte. In detail, a 5 L external reservoir containing 200 mM EFeMC (4.5 L) was connected to the cathodic chamber of the electrochemical cell in a flow cell configuration. 1% NO was purged into the reservoir at a flow rate of 5 L/min until NO@EFeMC reached the saturation concentration under anaerobic condition, and free NO was removed by purging Ar at a flow rate of 5 L/min. To determine saturation point, the concentration of NO emissions through the adsorption process was analyzed with a NO_X analyzer (MK 6000+, ECOM, Germany). The electrolyte prepared in a reservoir was circulated by a peristaltic pump at a flow rate of 20 mL/min during the electrochemical reduction of NO@EFeMC.

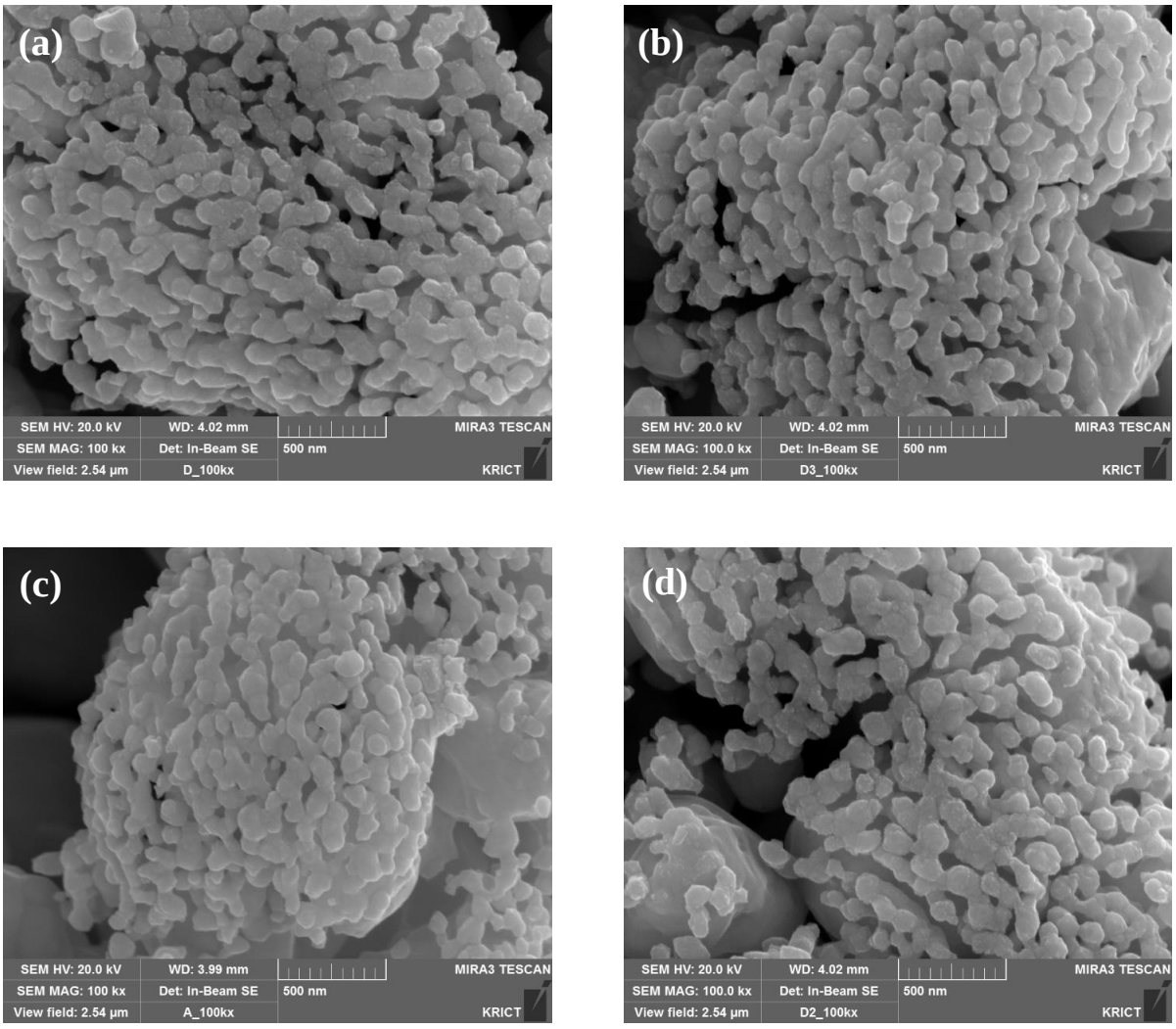

Figure S28. SEM images of Agn during the long-term test at different time intervals.
(a) 1 h, (b) 10 h, (c) 50 h, and (d) 100 h.

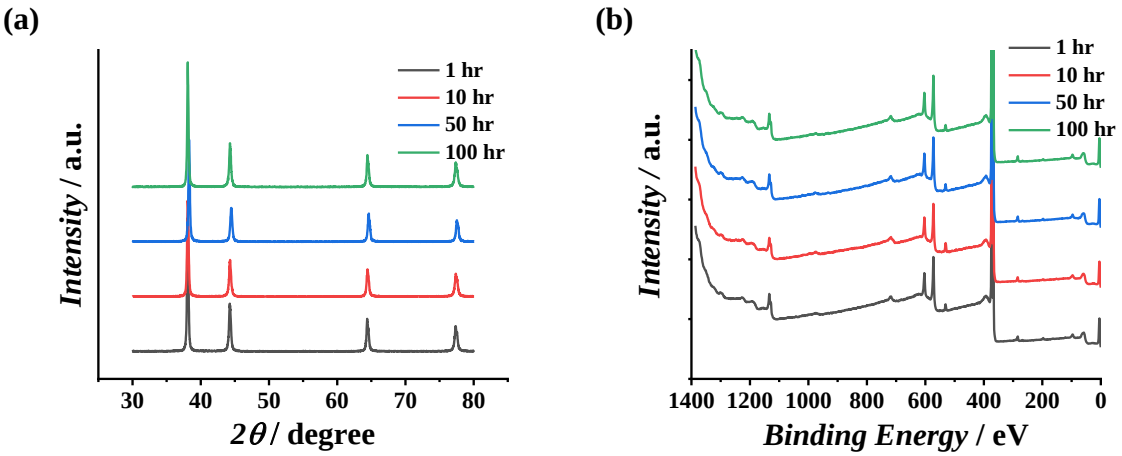

Figure S29. XRD profiles (a) and XPS spectra (b) of Agn during the long-term stability test.

Economic analysis

We carried out preliminary economic analysis of the electrochemical ammonia production process through itemized cost estimation compared with the market price of ammonia (0.56 \$ kg_{NH3}^{-1}) produced by the Haber–Bosch process. Based on the general economic analysis method reported by Turton et al., [9] the capital costs (electrolyzer and balance of plant) and operating costs (reactants, electricity, and maintenance) were estimated to calculate the unit ammonia production cost using the following equation.

$$Unit\ ammonia\ production\ cost\ (\$\ {kg_{NH3}}^{-1}) = \frac{Total\ annual\ costs\ (\$\ y^{-1})}{Annual\ ammonia\ production\ rate\ (kg_{NH3}\ y^{-1})}$$

The total annual cost is the sum of the annual capital cost and annual operating cost. The annual capital cost can be calculated by multiplying the capital cost by capital cost recovery (CRF) as follows:

$$CRF = \frac{i(1+i)^t}{(1+i)^t - 1},$$

where *i* is the discount rate (set as 4.5% in this study) and *t* is the equipment lifetime (set as 10 years in this study). A chemical engineering plant cost index of 603.1 is used to update the equipment cost from 2010 to 2018 (present).

Table S2. Assumptions for preliminary economic analysis [10]

Parameters	Value
Electrolyzer cost ($ m^{-2})	1,007
Balance of plant ($ y^{-1})	35% of the total cost of the electrolyzer system*
H_2O price	0.0054 $ gal^{-1}
Maintenance	2.5% of the electrolyzer cost

* The electrolyzer cost constitutes 65% of the total cost of the electrolyzer system.

Table S2 shows the assumptions for the preliminary economic analysis of the electrochemical ammonia production process from a previous report. [10] In addition, an electricity price of 0.07 $ kWh^{-1} is used. The price of NO as a reactant in the electrochemical ammonia production process is assumed zero because the NO capture cost and NO credit can be equivalent. In addition, it is assumed that an amount of NO used in the study is obtained from many power plants with various capacities because about 1,688 ton-NO y^{-1} is emitted for 67.5 MW power plant. [11] To calculate the current, electrolyzer area, power, and H_2O flow rate for itemized cost estimation, the following equations were used based on the report of Jouny et al. [10]

$$I\ (A) = \frac{PR\ x\ n_{NH3}\ x\ F}{MW_{NH3}\ x\ FE}$$

$$A\ (m^2) = \frac{I}{j}$$

$$P\ (kW) = I\ x\ V_{cell}$$

$$V_{cell}\ (V) = |V_{cathode} - V_{anode}|$$

$$FR_{H2O}\ (gal\ y^{-1}) = \frac{I\ x\ MW_{H2O}}{n_{H2O}\ x\ F}$$

Here, I is the current (A), PR is the production rate (150 million ton y^{-1}), n_{NH3} is the electron number for ammonia generation (5 mole e^-), F is the Faradaic constant (96,485.34 C/mole e^-), MW_{NH3} is the molar weight of ammonia (17.031 g mol^{-1}), FE is the Faradaic efficiency (99%), A is the electrolyzer area (m^2), j is the current density (48 mA cm^{-2}), P is the power (kW), V_{cell} is the cell voltage (V), $V_{cathode}$ is the cathodic potential (-0.165 V), V_{anode} is the anodic potential (1.5 V),[12] FR_{H2O} is the flow rate of H_2O (gal y^{-1}), MW_{H2O} is the molar weight of water (18.01528 g mol^{-1}), and n_{H2O} is the electron number of water (4 mole e^-).

Based on the aforementioned economic conditions, the itemized cost estimation for a unit ammonia production cost was obtained as shown in Table S3.

Table S3. Itemized cost estimation for a unit ammonia production cost with an annual ammonia production rate of 150 million tons y^{-1}

Item	Annual cost/ \$ y^{-1}	Ammonia production cost/ \$ kg_{NH3}^{-1}
Capital cost	55,512,038,917	0.37
Electrolyzer	36,082,825,296	0.24
Balance of plant	19,429,213,621	0.13
Operating cost	146,373,133,904	0.98
NO purchase	-	-
H_2O purchase	285,790,360	0.002
Electricity	138,949,512,854	0.93
Maintenance	7,137,830,690	0.05
Total cost	201,885,172,821	1.35

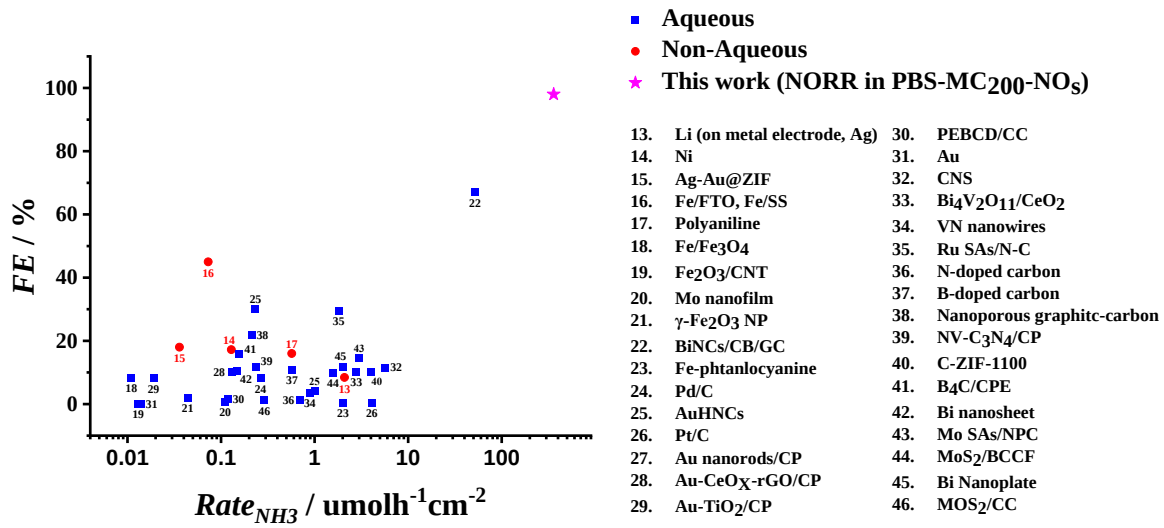

Figure S30. Comparison of the electrochemical ammonia production rates and Faradaic efficiencies of NORR in PBS-MC_{200}-NO_s electrolyte (this work) and the state-of-the-art NRR reported for various electrode materials and electrolytes [Ref. 13-46].

REFERENCES

1. Hsieh, Y.-C.; Senanayake, S. D.; Zhang, Y.; Xu, W.; Polyansky, D. E. Effect of chloride anions on the synthesis and enhanced catalytic activity of silver nanocoral electrodes for CO_2 electroreduction. *ACS Catal.* **2015**, *5*, 5349-5356.

2. Asadi, M.; Kim, K.; Liu, C.; Addepalli1, A. V.; Abbasi, P.; Yasaei, P.; Patrick, P.; Behranginia, A.; Cerrato, J. M,; Haasch, R.; Zapol, P.; Kumar, B.; Klie, R. F.; Abiade, J.; Curtiss, L. A.; Salehi-Khojin, A. Nanostructured transition metal dichalcogenide electrocatalysts for CO_2 reduction in ionic liquid. *Science* **2016**, 353, 467-470.

3. G. Kresse.; J. Furthmuller.; Efficient iterative schemes for ab initio total-energy calculations using a plane-wave basis set. *Phys. Rev. B.* **1996**, 54, 11169–11186.

4. J. P. Perdew.; K. Burke.; M. Ernzerhof.; Generalized gradient approximation made simple *Phys. Rev. Lett.* **1996**, 77, 3865–3868.

5. Zhao, Y.; Truhlar, D. G. The M06 suite of density functionals for main group thermochemistry, thermochemical kinetics, noncovalent interactions, excited states, and transition elements: two new functionals and systematic testing of four M06-class functionals and 12 other functionals. *Theor. Chem. Acc.* **2008**, *120*, 215-241.

6. Hay, P. J.; Wadt, W. R. *Ab initio* effective core potentials for molecular calculations. Potentials for K to Au including the outermost core orbitals. *J. Chem. Phys.* **1985**, *82*, 299.

7. Nørskov, J. K.; Rossmeisl, J.; Logadottir, A.; Lindqvist, L.; Kitchin, J. R.; Bligaard T.; Jónsson H. Origin of the overpotential for oxygen reduction at a fuel-cell cathode, *J. Phys. Chem. B* **2004**, *108*, 17886–17892.

8. Tawa, G. J.; Topol; I. A.; Burt, S. K.; Caldwell, R. A.; Rashin, A. A. Calculation of the aqueous solvation free energy of the proton. *J. Chem. Phys.* **1998**, *109*, 4852.

9. Turton, R.; Bailie, R. C.; Whiting, W. B.; Shaeiwitz, J. A.; Bhattacharyya, D. Analysis, synthesis, and design of chemical processes. *4th ed., New Jersey, Pearson* **2013**

10. Jouny, M.; Luc, W.; Jiao, F. General techno-economic analysis of CO_2 electrolysis systems. *Ind. Eng. Chem. Res.* **2018**, *57*, 2165.

11. Chakrabortya, N.; Mukherjeea, I.; Santraa, A.K.; Chowdhurya, S.; Chakraborty, S. Measurement of CO_2, CO, SO_2, and NO emissions from coal-based thermal power plants in India. *Atmos. Environ.* **2008**, 42, 1073-1082.

12. Bernt, M.; Siebel, A.; Gasteiger, H. A. Analysis of voltage losses in PEM water electrolyzer with low platinum group metal loadings. *J. Electrochem. Soc.* **2018**, *5*, F305-F314.

13. Tsuneto, A.; Kudo, A.; Sakata, T. Efficient electrochemical reduction of N_2 to NH_3 catalyzed by lithium. *Chem. Lett.* **1993**, *22*, 851-854.

14. Kim, K.; Yoo, C.-Y.; Kim, J.-N.; Yoon, H. C.; Han, J.-I. Electrochemical synthesis of ammonia from water and nitrogen in ethylenediamine under ambient temperature and pressure. *J. Electrochem. Soc.* **2016**, *163*, F1523-F1526.

15. Lee, H. K.; Koh, C. S. L.; Lee, Y. H.; Liu, C.; Phang, I. Y.; Han, X.; Tsung, C.-K.; Ling, X. Y. Favoring the unfavored: Selective electrochemical nitrogen fixation using a reticular chemistry approach. *Sci. Adv.* **2018**, *4*, eaar3208.

16. Zhou, F.; Azofra, L. M.; Ali, M.; Kar, M.; Simonov, A. N.; McDonnell-Worth, C.; Sun, C.; Zhang, X.; MacFarlane, D. R. Electro-synthesis of ammonia from nitrogen at ambient temperature and pressure in ionic liquids. *Energy Environ. Sci.* **2017**, *10*, 2516-2520.

17. Köleli, F.; Röpke, T. Electrochemical hydrogenation of dinitrogen to ammonia on a polyaniline electrode. *Appl. Catal. B* **2006**, *62*, 306-310.

18. Hu, L.; Khaniya, A.; Wang, J.; Chen, G.; Kaden, W. E.; Feng, X. Ambient electrochemical ammonia synthesis with high selectivity on Fe/Fe-oxide catalyst. *ACS Catal.* **2018**, *8*, 9312–9319.

19. Chen, S.; Perathoner, S.; Ampelli, C.; Mebrahtu, C.; Su, D.; Centi, G. Electrocatalytic synthesis of ammonia at room temperature and atmospheric pressure from water and nitrogen on a carbon-nanotube-based electrocatalyst. *Angew. Chem. Int. Ed.* **2017**, *56*, 2699–2703.

20. Yang, D.; Chen, T.; Wang, Z. Aqueous N_2 electrochemical reduction at low overpotential on (110)-oriented Mo nanofilm. *J. Mater. Chem. A.* **2017**, *5*, 18967–18971.

21. Kong, J.; Lim, A.; Yoon, C.; Jang, J. H.; Ham, H. C.; Han, J.; Nam, S.; Kim, D.; Sung, Y.-E.; Choi J.; Park, H. S. Electrochemical synthesis of NH_3 at low temperature and atmospheric pressure using a γ-Fe_2O_3 Catalyst. *ACS Sustain. Chem. Eng.* **2017**, *5*, 10986–10995.

22. Hao, Y.-C.; Guo, Y.; Chen, L.-W.; Shu, M.; Wang, X.-Y.; Bu, T.-A.; Gao, W.-Y.; Zhang, N.; Su, X.; Feng, X.; Zhou, J.-W.; Wang, B.; Hu, C.-W.; Yin, A.X.; Si, R.; Zhang, Y.-W.; Yan, C.-H. Promoting nitrogen electroreduction to ammonia with bismuth nanocrystals and potassium cations in water. *Nat. Catal.* **2018**, *2*, 448–456.

23. Furuya, N.; Yoshiba, H. Electroreduction of nitrogen to ammonia on gas diffusion electrodes modified by Fe-phthalocyanine. *J. Electroanal. Chem.* **1989**, *263*, 171-174.

24. Wang, J.; Yu, L.; Hu, L.; Chen, G.; Xin H.; Feng, X. Ambient ammonia synthesis via palladium-catalyzed electrohydrogenation of dinitrogen at low overpotential. *Nat. Commun.* **2018**, *9*, 1795.

25. Nazemi, M.; Panikkanvalappil, S. R.; El-Sayed, M. A. Enhancing the rate of electrochemical nitrogen reduction reaction for ammonia synthesis under ambient conditions using hollow gold nanocages. *Nano Energy* **2018**, *49*, 316-323.

26. Lan, R.; Irvine, J. T.; Tao, S. Synthesis of ammonia directly from air and water at ambient temperature and pressure. *Sci. Rep.* **2013**, *3*, 1145.

27. Bao, D.; Zhang, Q.; Meng, F.-L.; Zhong, H.-X.; Shi, M.-M.; Zhang, Y.; Yan, J.-M.; Jiang, Q.; Zhang, X.-B. Electrochemical reduction of N_2 under ambient conditions for

artificial N_2 fixation and renewable energy storage using N_2/NH_3 cycle. *Adv. Mater.* **2018**, *29*, 1604799.

28. Li, S.-J.; Bio, D.; Shi, M.-M.; Wulan, B.-R.; Yan J.-M.; Jiang, Q. Amorphizing of Au nanoparticles by CeO_x–RGO hybrid support towards highly efficient electrocatalyst for N_2 reduction under ambient conditions. *Adv. Mater.* **2017**, *29*, 1700001.

29. Shi, M.-M.; Bao, D.; Wulan, B. -R.; Li, Y.-H.; Zhang, Y.-F.; Yan, J.-M.; Jiang, Q. Au sub-nanoclusters on TiO_2 toward highly efficient and selective electrocatalyst for N_2 conversion to NH_3 at ambient conditions. *Adv. Mater.* **2017**, *29*, 1606550.

30. Chen, G.-F.; Cao, X.; Wu, S.; Zeng, X.; Ding, L.-X.; Zhu, M.; Wang, H. Ammonia electrosynthesis with high selectivity under ambient conditions via a Li^+ incorporation strategy, *J. Am. Chem. Soc.* **2017**, *74*, 9771-9774.

31. Yao, Y.; Zhu, S.; Wang, H.; Li, H.; Shao, M. A spectroscopic study on the nitrogen electrochemical reduction reaction on gold and platinum surfaces. *J. Am. Chem. Soc.* **2018**, *140*, 1496-1501.

32. Song, Y.; Johnson, D.; Peng, R.; Hensley, D. K.; Bonnesen, P. V.; Liang, L.; Huang, J.; Yang, F.; Zhang, F.; Qiao, R.; Baddorf, A. P.; Tschaplimski, T. J.; Engle, N. L.; Hatzell, M. C.; Wu, Z.; Cullen, D. A.; Meyer lll, H. M.; Sumpter, B. G.; Rondinone, A. J. A physical catalyst for the electrolysis of nitrogen to ammonia. *Sci. Adv.* **2018**, *4*, e1700336.

33. Lv, C.; Yan, C.; Chen, G.; Ding, Y.; Sun, J.; Zhou, Y.; Yu, G. An amorphous noble-metal-free electrocatalyst that enables nitrogen fixation under ambient conditions. *Angew. Chem. Int. Ed.* **2018**, *57*, 6073-6076.

34. Zhang, X.; Kong, R.-M.; Du, H.; Xia, L.; Qu, F. Highly efficient electrochemical ammonia synthesis via nitrogen reduction reactions on a VN nanowire array under ambient conditions. *Chem. Commun.* **2018**, *54*, 5323-5325.

35. Geng, Z.; Liu, Y.; Kong, X.; Li, P.; Li, K.; Liu, Z.; Du, J.; Shu, M.; Si, R.; Zeng, J. N_2 electrochemical reduction: achieving a record-high yield rate of 120.9 $\mu g NH_3\, mg cat.^{-1}\, h^{-1}$ for N_2 electrochemical reduction over Ru single-atom catalysts. *Adv. Mater.* **2018**, *30*, 1803498.

36. Liu, Y.; Su, Y.; Quan, X.; Fan, X.; Chen, S.; Yu, H.; Zhao, H.; Zhang, Y.; Zhao, J. Facile ammonia synthesis from electrocatalytic N_2 reduction under ambient conditions on N-doped porous carbon. *ACS Catal.* **2018**, *8*, 1186-1191.

37. Yu, X.; Han, P.; Wei, Z.; Huang, L.; Gu, Z.; Peng, S.; Ma, J.; Zheng, G. Boron-doped graphene for electrocatalytic N_2 reduction. *Joule* **2018**, *2*, 1610-1622.

38. Wang, H.; Wang, L.; Wang, Q.; Ye, S.; Sun, W.; Shao, Y.; Jiang, Z.; Qiao, Q.; Zhu, Y.; Song, P.; Li, D.; He, L.; Zhang, X.; Yuan, J.; Wu, T.; Ozin, G. A. Inside back cover: Ambient electrosynthesis of ammonia: electrode porosity and composition engineering. *Angew. Chem. Int. Ed.* **2018**, *57*, 12360.

39. Lv, C.; Qian, Y.; Yan, C.; Ding, Y.; Liu, Y.; Chen, G.; Yu, G. Defect engineering metal-free polymeric carbon nitride electrocatalyst for effective nitrogen fixation under ambient conditions. *Angew. Chem. Int. Ed.* **2018**, *57*, 10246.

40. Mukherjee, S.; Cullen, D. A.; Karakalos, S.; Liu, K.; Zhang, H.; Zhao, S.; Xu, H.; More, K. L.; Wang, G.; We, G. Metal-organic framework-derived nitrogen-doped highly disordered carbon for electrochemical ammonia synthesis using N_2 and H_2O in alkaline electrolytes. *Nano Energy* **2018**, *48*, 217-226.

41. Qiu, W.; Xie, X.-Y.; Qiu, J.; Fang, W.-H.; Liang, R.; Ren, X.; Ji, X.; Cui, G.; Asiri, A. M.; Cui, G.; Tang, B.; Sun, X. High-performance artificial nitrogen fixation at ambient conditions using a metal-free electrocatalyst. *Nat. Commun.* **2018**, *9*, 3485.

42. Li, L.; Tang, C.; Xia, B.; Jin, H.; Zheng, Y.; Qiao, S.-Z. Two-dimensional mosaic bismuth nanosheets for highly selective ambient electrocatalytic nitrogen reduction. *ACS Catal.* **2019**, *9*, 2902-2908.

43. Han, L.; Liu, X.; Chen, J.; Lin, R.; Liu, H.; Lu, F.; Bak, S.; Liang, Z.; Zhao, S.; Stavitski, E.; Luo, J.; Adzic, R. R.; Xin, H. L. Atomically dispersed molybdenum catalysts for efficient ambient nitrogen fixation. *Angew. Chem. Int. Ed.* **2019**, *58*, 2321-2325.

44. Liu, Y.; Han, M.; Xiong, Q.; Zhang, S.; Zhao, C.; Gong, W.; Wang, G.; Zhang, H.; Zhao, H. Ambient ammonia electrosynthesis: Dramatically enhanced ambient ammonia electrosynthesis performance by in-operando created Li–S interactions on MoS_2 electrocatalyst. *Adv. Energy Mater.* **2019**, *9*, 1803935.

45. Wang, Y.; Shi, M.-M.; Bao, D.; Meng, F.-L.; Zhang, Q.; Zhou, Y.-T.; Liu, K.-H.; Zhang, Y.; Wang, J.-Z.; Chen, Z.-W.; Liu, D.-P.; Jiang, Z.; Liu, M.; Gu, L.; Zhang, Q.-H.; Cao, X.-Z.; Yao, Y.; Shao, M.-H.; Zhang, Y.; Zhang, X.-B.; Chen, J. G.; Yan, J.-M.; Jiang, Q. Generating defect-rich bismuth for enhancing the rate of nitrogen electroreduction to ammonia. *Angew. Chem. Int. Ed.* **2019**, *58*, 9464-9469.

46. Zhang, L.; Ji, X.; Ren, X.; Ma, Y.; Shi, X.; Tian, Z.; Asiri, A. M.; Chen, L.; Tang, B.; Sun, X. Electrochemical ammonia synthesis via nitrogen reduction reaction on a MoS_2 catalyst: Theoretical and experimental studies. *Adv. Mater.* **2018**, *30*, e1800191.